

RESEARCH ARTICLE

Open Access



Compatible interface wave–structure interaction model for combining mesh-free particle and finite element methods

Naoto Mitsume¹

*Correspondence:
mitsume@kz.tsukuba.ac.jp

¹Faculty of Engineering,
Information and Systems,
University of Tsukuba, Tsukuba,
Japan

Abstract

This study presents a novel wave–structure interaction model, which is a compatible interface wave–structure interaction model that is based on mesh-free particle methods for free-surface flow analysis; the FEM for structural analysis. We adopt the explicitly represented polygon (ERP) wall boundary model, which is a polygon wall boundary model for mesh-free particle methods, to express the fluid–structure interfaces. The fluid–structure interfaces in the proposed model are geometrically compatible because the ERP model has advantages in dealing with complex-shaped and moving boundaries and it enables the direct use of surface meshes and shape functions given by finite element models of structures. This allows the automatic generation of polygons for free-surface flow analysis from finite elements, and therefore, it greatly increases the flexibility of the analysis. Based on the compatible interface between the polygons and finite elements, we propose a strong coupling algorithm based on an iterative partitioned scheme that defines the interacting models between the fluid and the structure. We model the force exerted by fluid particles on structures such that the kinetic boundary condition on the fluid–structure interface is satisfied. We perform the verification and validation tests of the proposed model by solving two benchmark problems.

Keywords: Finite element method, Mesh-free particle method, Fluid–structure interaction, Free-surface flow, Partitioned iterative coupling method

Introduction

A large tsunami can inflict devastating damage, as evidenced by the Great East Japan Earthquake and Tsunami that occurred on March 11, 2011. Severe accidents triggered by tsunamis such as the Fukushima Daiichi nuclear disaster have the potential to cause catastrophic harm to people; this has led to an increased awareness regarding the vital importance of designing safe, tsunami-resistant structures (including the buildings and machinery of electric power, energy, and chemical plants) and evacuation facilities in coastal regions.

Thus far, several experimental studies have evaluated pressure forces generated by tsunamis and proposed practical experimental formulas [1–3]. These Experimental formulas for estimating collision forces attributed to floating debris [4,5] have also been presented. Although these formulas are very useful in the design process of defense structures such as levees, numerical analyses can be considered viable alternatives. Two-dimensional wave models, as represented by the shallow-water equations and Boussinesq-type wave models, have been used to understand large-scale wave behaviors [6–8] because these models can save computational costs compared to that incurred by running direct simulations of the three-dimensional Navier–Stokes equations. The inundation area for tsunamis can be predicted using an appropriate representation of bottom friction, Coriolis force, and any other parameter [9]. In contrast with the two-dimensional numerical simulations, direct simulations based on Navier–Stokes equations [10–12] have been conducted to assess wave forces exerted by tsunamis. Although these simulations can consider the three-dimensional nature of waves accurately, they often incur considerably high computational costs for computing large-scale wave behaviors. A multiscale approach to wave modeling is employed to reduce the computational burden; this approach exploits both the two- and three-dimensional computations. For example, a combination of the two-dimensional shallow-water equations and three-dimensional Navier–Stokes equations [13–16] has recently attracted considerable research attention.

Although existing studies have played an important role in tsunami disaster prevention, it is sometimes economically impossible to mitigate all the deleterious effects of such disasters. Therefore, structural design that is resilient to the catastrophic damage incurred by tsunamis, i.e., structural design that can maintain functions even for beyond-the-design-basis conditions [17] has recently gained increasing attention. Damage created by a tsunami is attributed to many factors: the direct force of the wave, elastic and plastic deformation, collisions with floating debris, and buoyancy [18]. All these factors must be considered when developing tsunami-resilient designs; however, it is difficult to predict them using conventional processes that are based only on empirical knowledge and wave simulations. An integrative strategy that includes the wave–structure interaction analysis is a powerful and important part of the tsunami-resilient design processes.

The wave–structure interaction problem can be considered a type of fluid–structure interaction (FSI) problem with free surfaces. Considerable research has been conducted to solve FSI problems using the finite element method (FEM). Given the high accuracy and widespread application of the FEM, it is the de facto standard method for structural analysis. However, the analysis of free-surface flow using FEM is not straightforward. Interface capturing methods such as the volume of fluid method [19] and the level set method [20,21] use an artificial scalar field to describe the interfaces implicitly. These approaches can perform robust calculations even if the interfaces are subjected to severe motion caused by topological changes. However, the interface capturing methods suffer from mass conservation and interface smearing problems. In addition to the above approaches, which are Eulerian or ALE formulations in fluids, the particle FEM (PFEM) [22–26] uses Lagrangian formulations in the fluid and eliminates the problems of free surfaces and moving boundaries. However, PFEM requires frequent remeshing.

In contrast with mesh-based methods, mesh-free particle methods such as smoothed particle hydrodynamics (SPH) [27,28] and moving particle semi-implicit/simulation (MPS) [29] are inherently Lagrangian methods wherein a continuum is discretized as

a group of moving particles. These methods continue to clearly define moving boundaries that include free surfaces even during long analyses because of their Lagrangian formulations. Coupled analyses that include a fluid-rigid body and fluid–structure interactions have been conducted using mesh-free particle methods [30–33]. However, these methods are less accurate on solid surfaces and have limited applicability to structural analysis, such as with the finite difference method, because the Neumann boundary conditions on solid surfaces must be explicitly imposed and the derivatives need to be approximated by particles within the circular support domain unlike the FEM, which solves weak form equations.

Hybrid coupled models that use mesh-free particle methods and FEM have been proposed to exploit the advantages of both methods. Early studies on coupled analysis related to these models [34–39] were conducted to deal with large deformation, penetration, crack propagation, and fragmentation, wherein structure–structure interaction problems were solved. Existing studies on FSI analyses using the FEM and the particle methods [40–43], in which commercial programs such as the PAM-CRASH and LS-DYNA are often used, have also been conducted. In recent years, existing studies on modeling the hybrid FSI model [42, 44–49] have focused on approaches to formulate interactions between the free-surface flow computation based on particle methods and the structural computation based on the FEM. Lee et al. [45] developed a partitioned coupled FSI model between the MITC4 shell element based on structural computation and the MPS based free-surface flow computation, wherein wall particles and nodes of the shell elements overlapped to exchange physical values. Fourey et al. [42] proposed a model between the SPH method with the ghost particle model as a wall boundary model and the FEM. They obtained force from fluid to structure via the surface integration of pressures on the fluid–structure interface interpolated by the weighted average of pressures on the neighboring particles. Yang et al. [49, 50] developed a model using the SPH method and the FEM. As with the Lee’s study, the wall particles and nodes of the finite elements were overlapped at the same positions, and the force exerted on the surface of the structure was obtained considering the reaction forces in the fluid computation. They conducted computations for quantitative validation compared with experimental results. Thiyahuddin et al. [48] developed a model using the SPH method and the FEM to solve for a car colliding with water-filled barriers. They modeled the fluid–structure interface with a finite thickness for preventing the penetrations of particles into structures. Recently, Li et al. [46, 47] proposed a partitioned coupled FSI model between the FEM and SPH-ALE method [51]. They discussed the nonphysical creation and dissipation of energy on the fluid–structure interface and developed a formulation to prevent it. However, these hybrid coupled models have mainly employed weak coupling schemes based on staggered algorithms such as the conventional serial staggered (CSS) scheme, and do not implicitly treat fluid–structure interfaces.

Similar to this trend, we developed MPS-FE methods [52–54] that adopts the MPS method for fluid computation involving free surfaces and the FEM for structure computation. These two methods are coupled with a partitioned approach, i.e., the CSS scheme [55], which can set different time step sizes for the fluid and structure computations. The method combines advantages of both methods for achieving efficiency and robustness. However, the conventional MPS-FE method in which the MPS wall boundary particles and finite elements are overlapped to exchange information on fluid–structure interfaces cannot deal with complex-shaped fluid–structure boundaries because the wall particles need

to be set in an orthogonal and uniform grid manner for the accurate execution of the MPS computation. This requires cumbersome interpolation for the exchange of physical values based on the node-particle correspondence relation. Therefore, the MPS-FE method lacks versatility and reduces software modularity. Further, forces on fluid-structure interfaces are not balanced when the pressure on the walls is calculated in this manner.

This study presents a novel wave-structure interaction model, which is a compatible interface-structure interaction model that is based on mesh-free particle methods for free-surface flow analysis; the FEM for structural analysis. We adopt the explicitly represented polygon (ERP) wall boundary model [56], which is a polygon wall boundary model for mesh-free particle methods, to express the fluid-structure interfaces. The fluid-structure interfaces in the proposed model are geometrically compatible because the ERP model has advantages in dealing with complex-shaped and moving boundaries and it enables the direct use of surface meshes and shape functions given by finite element models of structures. This allows the automatic generation of polygons for free-surface flow analysis from finite elements, and therefore, it greatly increases the flexibility of the analysis. Detailed formulations of the ERP model introduced to the explicit MPS method, which is a mesh-free particle method with explicit pressure calculation, is described in “Free-surface flow analysis by explicit moving particle simulation (MPS) method with explicitly represented polygon (ERP) wall boundary model”. In order to map physical quantities between particle methods for strong-form equations and finite element methods for weak-form equations, we propose a novel formulation based on the Dirac delta function, where the force exerted on the structure by each fluid particle is considered as a point load. It is formulated such that the kinetic boundary condition on the fluid-structure interface is satisfied. In addition, we introduce a strong coupling algorithm based on an iterative partitioned scheme to discuss its effect on numerical results and the convergence of iterations, which has not been discussed much in existing studies on the hybrid coupled models. The details on these procedures are introduced in “Verification and validation”. We perform the verification and validation tests of the proposed model by solving two benchmark problems. First, we solve a dam break problem with an elastic obstacle; the result of the proposed model are compared those of one of the several existing studies. Then, we simulate the experiment of a sloshing tank with an elastic beam; these test cases are then introduced in “Conclusions”.

Governing equations of fluid-structure interaction (FSI) problem with free surfaces

Definition of spaces

Figure 1 shows the spaces and boundaries in an FSI problem involving free surfaces. The whole area of the fluid-structure interaction analysis, Ω , which is partitioned into areas of free-surface flow analysis and structural analysis, $\Omega_{\mathcal{F}}$ and $\Omega_{\mathcal{S}}$, respectively, is given as

$$\Omega = \Omega_{\mathcal{F}} \cup \Omega_{\mathcal{S}}. \quad (1)$$

The boundaries of the free-surface flow and structural analyses are denoted as $\Gamma_{\mathcal{F}}$ and $\Gamma_{\mathcal{S}}$, respectively.

The domain of the free-surface flow analysis is partitioned into the fluid domain, $\Omega_{\mathcal{F},F}$, and the other domain, $\Omega_{\mathcal{F},V}$. A free-surface boundary, $\Gamma_{\mathcal{F},FS}$, is defined between these

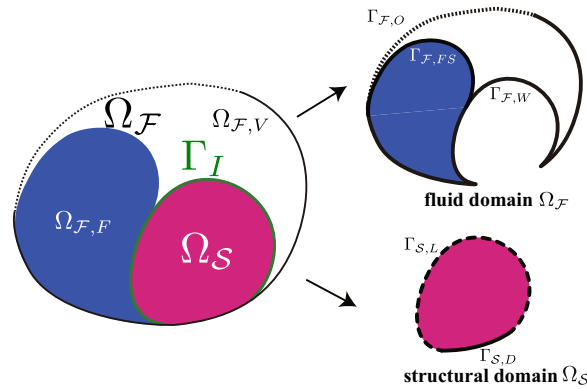


Fig. 1 Schematic of the fluid–structure interaction problem with free surface

two domains. In this study, we consider the open boundary, $\Gamma_{F,O}$, and wall boundary, $\Gamma_{F,W}$, on the boundary of the free-surface flow analysis. We do not consider inflow boundaries in this study. The domain of structural analysis is partitioned into boundaries with displacement and traction boundary conditions, $\Gamma_{S,D}$ and $\Gamma_{S,L}$, respectively.

Let Γ_I represent the fluid–structure interface. Then, the FSI boundaries in the free-surface flow and structural analyses denoted as, $\Gamma_{F,I}$ and $\Gamma_{S,I}$, can be considered different.

Governing equations and boundary conditions

The governing equations in both the fluid and the structure are Cauchy’s 1st law of motion,

$$\frac{D}{Dt}(\rho \mathbf{v}) = \nabla \cdot \boldsymbol{\sigma} + \rho \mathbf{g}, \tag{2}$$

where $\frac{D}{Dt}$, ρ , \mathbf{v} , $\boldsymbol{\sigma}$, and \mathbf{g} represent the material derivative, density, velocity vector, Cauchy stress tensor, and gravitational acceleration vector, respectively.

In our FSI problem, the constitutive laws in the fluid and structure in terms of stress are different. Let $\boldsymbol{\sigma}^F$ and $\boldsymbol{\sigma}^S$ represent the stress tensors in the fluid and structural analyses, respectively.

$$\boldsymbol{\sigma}^F = -p\mathbf{I} + \mu \left(\nabla \mathbf{v} + (\nabla \mathbf{v})^T \right) \quad \text{in } \Omega_{F,F}, \tag{3}$$

$$\boldsymbol{\sigma}^S = \frac{1}{\det \mathbf{F}} \mathbf{F} \mathbf{S} \mathbf{F}^T \quad \text{in } \Omega_S, \tag{4}$$

where p , μ , \mathbf{F} , and \mathbf{S} represent the pressure, viscosity, deformation gradient tensor, and 2nd Piola–Kirchhoff stress tensor, respectively.

On the fluid–structure interface, the following geometric and kinetic boundary conditions need to be imposed.

$$\mathbf{v}^F - \mathbf{v}^S = \mathbf{0} \quad \text{on } \Gamma_I, \tag{5}$$

$$\boldsymbol{\sigma}^F \mathbf{n}^F + \boldsymbol{\sigma}^S \mathbf{n}^S = \mathbf{0} \quad \text{on } \Gamma_I, \tag{6}$$

where \mathbf{v}^F and \mathbf{v}^S represent the velocities in the fluid and structure domain, and \mathbf{n}^F and \mathbf{n}^S represent the outward unit normal vectors in the fluid and structure domains.

Table 1 Definition of indices for the formulation of compatible interface wave–structure interaction model

Fluid particle:	i	$(i \in \Lambda_{\text{particle}} = \{1, \dots, N_{\text{particle}}\})$
Neighboring particle within effective radius:	j	
Polygon wall:	s	$(s \in \Lambda_{\text{pol}} = \{1, \dots, N_{\text{pol}}\})$
Polygon wall on the fluid–structure (FS) interface:	\tilde{s}	$(\tilde{s} \in \tilde{\Lambda}_{\text{pol}} \subset \Lambda_{\text{pol}})$
Global node of the polygon wall:	L	$(L \in \Lambda_{\text{pnode}} = \{1, \dots, N_{\text{pnode}}\})$
Global node of the polygon wall on the FS interface:	\tilde{L}	$(\tilde{L} \in \tilde{\Lambda}_{\text{pnode}} \subset \Lambda_{\text{pnode}})$
Finite element (FE):	e	$(e \in \Lambda_{\text{elem}} = \{1, \dots, N_{\text{elem}}\})$
FE surface:	b	$(b \in \Lambda_{\text{surface}} = \{1, \dots, N_{\text{surface}}\})$
FE surface on the FS interface:	\tilde{b}	$(\tilde{b} \in \tilde{\Lambda}_{\text{surface}} \subset \Lambda_{\text{surface}})$
Global node of FE:	K	$(K \in \Lambda_{\text{fnode}} = \{1, \dots, N_{\text{fnode}}\})$
Global node of the FE on the FS interface:	\tilde{K}	$(\tilde{K} \in \tilde{\Lambda}_{\text{fnode}} \subset \Lambda_{\text{fnode}})$
Timestep:	n	$(1 \leq n \leq N_{\text{timestep}})$

Rule of indices

The FSI model has many ingredients such as fluid particles, polygon walls, finite elements, and nodes. For the ease of formulation, we adopt a rule in which each character used as an index with a physical value specifies an ingredient the value is defined on, as indicated in Table 1. In this table, Λ represents index set.

Free-surface flow analysis by explicit moving particle simulation (MPS) method with explicitly represented polygon (ERP) Wall Boundary Model

Governing equations

Substituting Eq. (3) into Eq. (2) produces the Navier–Stokes equations in a Lagrangian reference frame as

$$\frac{D\mathbf{v}}{Dt} = -\frac{1}{\rho}\nabla p + \nu\nabla^2\mathbf{v} + \mathbf{g}, \tag{7}$$

where p represents the pressure and ν represents the kinetic viscosity defined as $\nu = \frac{\mu}{\rho}$.

Differential operator models in MPS method

In the MPS discretization, the differential operators acting on particle i are evaluated using neighboring particles, j , located within an effective radius, r_e .

The neighboring particles are weighted by a function with respect to the relative distance, r . In this study, we use the quadratic function

$$w(r) = \begin{cases} \left(\frac{r}{r_e} - 1\right)^2 & (0 \leq r < r_e) \\ 0 & (r_e \leq r). \end{cases} \tag{8}$$

The normalization factor, called the particle number density, is defined as

$$n_i = \sum_{\substack{j=1 \\ j \neq i}}^{N_{\text{particle}}} w(|\mathbf{x}_j - \mathbf{x}_i|), \tag{9}$$

where N_{particle} represents the number of particles. The particle number density is proportional to the density of the fluid.

In the EMPS method, differential operators in the governing equations are computed as

$$\langle \nabla p \rangle_i = \frac{d}{n^0} \sum_{\substack{j=1 \\ j \neq i}}^{N_{\text{particle}}} \left[\frac{(p_j + p_i)(\mathbf{x}_j - \mathbf{x}_i)}{|\mathbf{x}_j - \mathbf{x}_i|^2} w(|\mathbf{x}_j - \mathbf{x}_i|) \right], \tag{10}$$

$$\langle \nabla^2 \mathbf{v} \rangle_i = \frac{2d}{\lambda^0 n^0} \sum_{\substack{j=1 \\ j \neq i}}^{N_{\text{particle}}} [(\mathbf{v}_j - \mathbf{v}_i) w(|\mathbf{x}_j - \mathbf{x}_i|)]. \tag{11}$$

Here, d , n^0 , and $\langle \rangle$ represent the number of dimensions, initial value of the particle number density given by Eq. (9) and calculated for the initial particle geometry, and discretization by the MPS differential model, respectively. Further, λ^0 represents a correction parameter, which ensures that the increase in the variance is equal to that of the analytical solution; like n^0 , it is calculated for the initial geometry as

$$\lambda_i = \frac{1}{n_i} \sum_{\substack{j=1 \\ j \neq i}}^{N_{\text{particle}}} |\mathbf{x}_j - \mathbf{x}_i|^2 w(|\mathbf{x}_j - \mathbf{x}_i|). \tag{12}$$

Time-stepping algorithm in the EMPS method

In the original MPS method [29], the fractional step method is applied for time discretization; this method splits each time step into two pseudo-time steps of prediction and correction. Therefore, the velocity in the new time step $n + 1$ is given by the sum of the predicted velocity, \mathbf{v}^* , and the velocity correction value, \mathbf{v}' , as $\mathbf{v}^{n+1} = \mathbf{v}^* + \mathbf{v}'$. The predicted velocity \mathbf{v}^* is explicitly calculated using viscosity terms and source terms as

$$\frac{\mathbf{v}_i^* - \mathbf{v}_i^n}{\Delta t} = \nu \langle \nabla^2 \mathbf{v} \rangle_i^n + \mathbf{g}. \tag{13}$$

Next, the velocity at $n + 1$ step is given by

$$\frac{\mathbf{v}_i^{n+1} - \mathbf{v}_i^*}{\Delta t} = -\frac{1}{\rho} \langle \nabla p \rangle_i^{n+1}. \tag{14}$$

Although the original MPS method solves the pressure Poisson equation implicitly, the EMPS method [57,58] explicitly calculates the pressure by introducing a pseudo-compressibility. The pressure is calculated as

$$p_i^{n+1} = c^2 \frac{\rho}{n_0} (n_i^* - n_0), \tag{15}$$

where c represents the speed of sound, which can be set arbitrarily to satisfy the condition of stability and incompressibility.

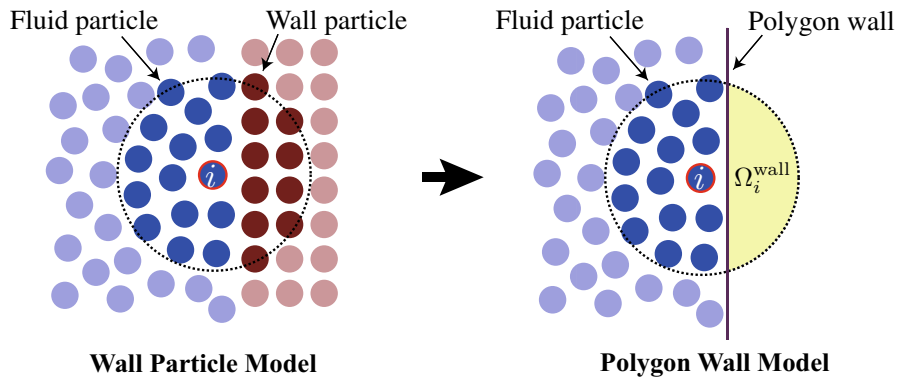


Fig. 2 Schematic of the conventional wall model that represents wall boundaries as particles (wall particle model) and the polygon wall boundary model

Free-surface criterion

For particles on a free surface, $\Gamma_{\mathcal{F},FS}$, we apply the Dirichlet condition for the pressure, $p = 0$. This is a simple approximation of the free-surface condition.

$$\sigma^F \mathbf{n}^F = \mathbf{0} \quad \text{on } \Gamma_{\mathcal{F},FS}. \tag{16}$$

The condition for free-surface particle recognition is given as

$$n_i^* < \beta n_0, \tag{17}$$

where β represents a threshold coefficient. In the EMPS model, we set $\beta = 1.0$ to prevent instability caused by tensile stress.

ERP wall boundary model

Polygon detection

The ERP model [56] expresses the wall boundaries as polygons, which are explicitly represented without using the signed distance function; we assume that each fluid particle is affected by only the nearest polygon. Here, we denote the nearest points on each polygon wall s from the particle i as $\mathbf{x}_{i,s}^{\text{near}}$. The closest point, $\mathbf{x}_i^{\text{wall}}$, for all $\mathbf{x}_{i,s}^{\text{near}}$ is defined as

$$\mathbf{x}_i^{\text{wall}} = \underset{\mathbf{x}_{i,s}^{\text{near}}}{\operatorname{argmin}} |\mathbf{x}_i - \mathbf{x}_{i,s}^{\text{near}}| \quad (s = 1, 2, \dots, N_{\text{pol}}), \tag{18}$$

where N_{pol} represents the number of polygons. The outward unit normal vector at $\mathbf{x}_{i,s}^{\text{near}}$ is defined as

$$\mathbf{n}_i^{\text{wall}} = \frac{\mathbf{x}_i - \mathbf{x}_i^{\text{wall}}}{|\mathbf{x}_i - \mathbf{x}_i^{\text{wall}}|}. \tag{19}$$

Corrections of particle number density

Figure 2 shows that the conventional wall model for the MPS method [29] represents wall boundaries as particles (wall particles). Although the ERP model does not require these wall particles, the particle number density inside the wall region shown in Fig. 2, Ω_i^{wall} , needs to be computed. The wall weight function, $z(r)$, is computed to interpolate this

value in the preprocessing stage (For details on the wall weight function, see [56,59]). The particle number density in the ERP model, n_i^{ERP} , which is used instead of Eq. (9), is computed as

$$n_i^{\text{ERP}} = n_i + z(|\mathbf{x}_i^{\text{wall}} - \mathbf{x}_i|). \tag{20}$$

Corrections of differential operators

The ERP model can impose the pressure Neumann and slip/no-slip boundary conditions in a similar manner to a ghost particle approach [60–64] that does not use ghost particles. We define the reflectional transformation matrix for particle i across its nearest polygon whose unit normal vector is $\mathbf{n}_i^{\text{wall}}$ as $\mathbf{R}_i^{\text{ref}}$, and for the inverse transformation matrix, \mathbf{R}^{inv} , as

$$\mathbf{R}_i^{\text{ref}} = \mathbf{I} - 2\mathbf{n}_i^{\text{wall}} \otimes \mathbf{n}_i^{\text{wall}}, \tag{21}$$

$$\mathbf{R}^{\text{inv}} = -\mathbf{I}, \tag{22}$$

and the mirroring position corresponding to particle i , $\mathbf{x}_{i'}$, as

$$\mathbf{x}_{i'} = \mathbf{x}_i + 2(\mathbf{x}_i^{\text{wall}} - \mathbf{x}_i), \tag{23}$$

where \mathbf{I} represents the second-order identity tensor, and $\mathbf{x}_{i'}$ represents the mirroring position of \mathbf{x}_i .

For the no-slip boundary condition, the following differential operator model for the Laplacian of the velocity is used instead of Eq. (11).

$$\begin{aligned} \langle \nabla^2 \mathbf{v} \rangle_i^{\text{ERP}} &= \langle \nabla^2 \mathbf{v} \rangle_i + \mathbf{R}^{\text{inv}} \langle \nabla^2 \mathbf{v} \rangle_{i'}, \\ \mathbf{v}_{i'} &= \mathbf{R}^{\text{inv}} \left[\mathbf{v}_i - 2 \left\{ \mathbf{v}_i^{\text{wall}} - \left(\mathbf{n}_i^{\text{wall}} \cdot \mathbf{v}_i^{\text{wall}} \right) \mathbf{n}_i^{\text{wall}} \right\} \right], \end{aligned} \tag{24}$$

where $\mathbf{v}_i^{\text{wall}}$ represents the velocity of the wall at $\mathbf{x}_i^{\text{wall}}$.

The following differential operator model for the pressure gradient is used instead of Eq. (10) to impose the pressure Neumann boundary condition on the wall; this condition corresponds to the slip boundary condition.

$$\langle \nabla p \rangle_i^{\text{ERP}} = \langle \nabla p \rangle_i + \mathbf{R}_i^{\text{ref}} \langle \nabla p \rangle_{i'} + \mathbf{f}_i^{\text{rep}}, \tag{25}$$

$$p_{i'} = p_i \tag{26}$$

where the second and third terms are additional terms in the ERP model, and $\mathbf{f}_i^{\text{rep}}$ represents the repulsive force term for preventing penetrations at curved edges. An earlier study [56] used the repulsive force

$$\mathbf{f}_i^{\text{rep}} = \begin{cases} -\alpha^{\text{rep}} \left(\frac{\frac{1}{2}l^0}{r} - 1 \right) \mathbf{n}_i^{\text{wall}} & (0 \leq r < \frac{1}{2}l^0) \\ 0 & (\frac{1}{2}l^0 \leq r) \end{cases}, \tag{27}$$

which has a parameter α^{rep} .

Structural analysis using the finite element method (FEM)

Weak form of governing equation

In the structural analysis, we determine the displacement, \mathbf{u} , and velocity, \mathbf{v} , as

$$\mathbf{u} = \mathbf{x} - \mathbf{X}, \tag{28}$$

$$\mathbf{v} = \frac{D\mathbf{u}}{Dt}, \tag{29}$$

where \mathbf{X} represents a point in the reference configuration and \mathbf{x} represents one in the current configuration. The deformation gradient tensor, \mathbf{F} , is defined as the linear operator between infinitesimal fibers in the reference and the current configurations.

$$\mathbf{F} = \frac{d\mathbf{x}}{d\mathbf{X}} = \nabla_{\mathbf{X}}\mathbf{x}. \tag{30}$$

Based on the weighted residual method with the weight function, \mathbf{W} , the weak form of the governing equation (Eq. (2)) in the current configuration, can be written as

$$\int_{\Omega_S} \frac{D}{Dt}(\rho\mathbf{v}) \cdot \mathbf{W} d\Omega + \int_{\Omega_S} \boldsymbol{\sigma}^F : \boldsymbol{\epsilon}(\mathbf{W}) d\Omega = \int_{\Omega_S} \rho\mathbf{g} \cdot \mathbf{W} d\Omega + \int_{\Gamma_I} \boldsymbol{\sigma}^S \mathbf{n}^S \cdot \mathbf{W} d\Gamma, \tag{31}$$

$$\boldsymbol{\epsilon}(\mathbf{W}) = \frac{1}{2} \left(\nabla \mathbf{W} + (\nabla \mathbf{W})^T \right). \tag{32}$$

Here, we assume that the traction boundary excluding the fluid–structure interface is imposed on the traction-free condition

$$\boldsymbol{\sigma}^S \mathbf{n}^S = \mathbf{0} \quad \text{on } \Gamma_{S,L} \setminus \Gamma_I. \tag{33}$$

This study uses the following Saint Venant–Kirchhoff model as a constitutive law of structures.

$$\mathbf{S} = \frac{\partial W(\mathbf{E})}{\partial \mathbf{E}}, \tag{34}$$

$$W(\mathbf{E}) = \frac{\lambda^S}{2} (\text{tr} \mathbf{E})^2 + \mu^S \text{tr}(\mathbf{E}^2), \tag{35}$$

$$\mathbf{E} = \frac{1}{2} \left(\nabla_{\mathbf{X}} \mathbf{u} + (\nabla_{\mathbf{X}} \mathbf{u})^T + (\nabla_{\mathbf{X}} \mathbf{u})(\nabla_{\mathbf{X}} \mathbf{u})^T \right), \tag{36}$$

where \mathbf{E} , $W(\mathbf{E})$, and λ^S and μ^S represent the Green–Lagrange strain tensor, strain energy density function, and Lamé’s constants, respectively.

Spatial discretization based on the Galerkin method

Equation (31) is discretized using the Galerkin method. The weight function and displacement are approximated as

$$\mathbf{W}(\mathbf{x}) \simeq \sum_{K=1}^{N_{\text{fnode}}} \mathbf{W}_K N_K(\mathbf{x}), \tag{37}$$

$$\mathbf{u}(\mathbf{x}) \simeq \sum_{K=1}^{N_{\text{fnode}}} \mathbf{u}_K N_K(\mathbf{x}), \tag{38}$$

where W_K and u_K represent values of the weight function and the displacement at node K , respectively; N_{node} represents the number of nodes, and $N_K(\mathbf{x})$ represents the shape function of node K . We assume that the shape function used here satisfies the partition of the unity condition at any $\mathbf{x} \in \Omega_S$,

$$\sum_{K=1}^{N_{\text{node}}} N_K(\mathbf{x}) = 1. \quad (39)$$

This study adopts an isoparametric 2nd-order triangle element whose shape function satisfies this condition.

Time integration scheme

Newmark's β method is used as the time integration scheme in this study [65].

$$\mathbf{u}^{n+1} = \mathbf{u}^n + \Delta t \mathbf{v}^n + \left(\frac{1}{2} - \beta\right) \Delta t^2 \mathbf{a}^n + \beta_{\text{NB}} \Delta t^2 \mathbf{a}^{n+1}, \quad (40)$$

$$\mathbf{v}^{n+1} = \mathbf{v}^n + (1 - \gamma_{\text{NB}}) \Delta t \mathbf{a}^n + \gamma_{\text{NB}} \Delta t \mathbf{a}^{n+1}, \quad (41)$$

where β_{NB} and γ_{NB} are the coefficients. Although the coefficients are decided within the ranges of the Von-Neumann stability criteria, other parameter sets, which generate numerical damping, are sometimes used for stability in a positive manner [66–68]. This study adopts $\beta_{\text{NB}} = 0.3025$ and $\gamma_{\text{NB}} = 0.6$, which generates numerical damping for stable computations.

Nonlinear and linear solvers

The discretized equation given by Eq. (31) with Eqs. (37), (38), (40), and (41) is still nonlinear. This study uses the Newton–Raphson method for the linearization of this equation, and the conjugate gradient method as the linear solver.

Compatible interface wave–structure interaction model

We present an FSI model—the compatible interface wave–structure interaction model—based on the EMPS method for free-surface flow computation and the FEM for structure computation. The ERP model is adopted to represent the fluid–structure interface as illustrated in Fig. 3. This model is formulated to exploit the advantages of both methods when dealing with complicated phenomena including moving boundaries and structures with various types of constitutive laws. In the proposed model, fluid–structure interfaces are geometrically compatible because the ERP wall boundary model allows us to use surfaces of finite elements directly as wall boundaries in computation of the free-surface flow. In addition, the force exerted by fluid particles on structures is modeled such that the kinetic boundary condition on the fluid–structure interface is satisfied.

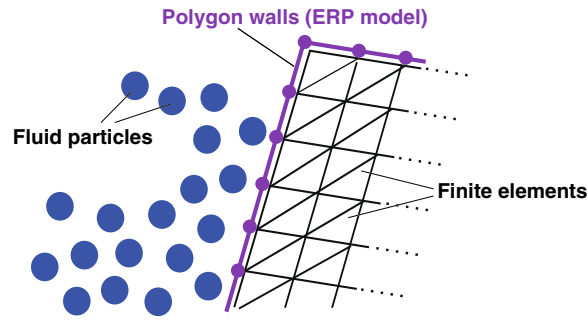


Fig. 3 Schematic of the compatible interface wave–structure interaction model between the finite element

Approximations of the fluid and structure domains

Fluid domain represented by fluid particles in particle methods

The fluid domain at $t = 0$, $\Omega_{\mathcal{F},F}^0$, is approximated by fluid particles, each of which has its own volume and space, as

$$\Omega_{\mathcal{F},F}^0 \simeq \bigcup_{i=1}^{N_{\text{particle}}} \Omega_i^0. \tag{42}$$

However, unlike the mesh-based methods, the particle methods do not have connectivity information, and therefore, the area of the particle i , Ω_i , is not clearly specified.

Although different volumes of particles can be used [69, 70], computations using particle methods assume that all particles have the same volume. This study also adopts the same assumption. Assuming that fluid particles are set in a uniform grid in the initial configuration and the initial particle spacing is l^0 , the volume and mass of a particle i are given as

$$V_i = (l^0)^d, \tag{43}$$

$$m_i = \rho V_i. \tag{44}$$

Wall boundary represented by the polygon walls of the ERP model

The ERP wall boundary model approximates the wall boundary at $t = 0$, $\Omega_{\mathcal{F},F}^0$ by polygon walls as

$$\Gamma_{\mathcal{F},W}^0 \simeq \bigcup_{i=1}^{N_{\text{pol}}} \Gamma_s^0. \tag{45}$$

The shape function in the FEM is defined on each polygon and node.

Structural domain represented by finite elements

When computing a structure based on the FEM, the structural domain at $t = 0$, Ω_S^0 , is approximated by finite elements as

$$\Omega_S^0 \simeq \bigcup_{i=1}^{N_{\text{elem}}} \Omega_e^0, \tag{46}$$

where N_{elem} represents the number of finite elements.

Correspondence relation between the polygon walls and finite elements

In the structural computation, finite elements represent the fluid–structure interface, $\Gamma_{S,I}$, as their surfaces,

$$\Gamma_{\mathcal{F},I}^0 \simeq \bigcup_{\tilde{s} \in \tilde{\Lambda}_{\text{pol}}} \Gamma_{\tilde{s}}^0. \tag{47}$$

The polygon walls for the ERP model can be obtained by the surface traction of the finite elements, which approximates the fluid–structure interface, $\Gamma_{\mathcal{F},I}$, as

$$\Gamma_{S,I}^0 \simeq \bigcup_{\tilde{b} \in \tilde{\Lambda}_{\text{surface}}} \Gamma_{\tilde{b}}^0. \tag{48}$$

If the same shape functions are used, the polygon walls generated by the surface extraction are compatible to the finite elements

$$\Gamma_I \simeq \Gamma_{S,I} \simeq \Gamma_{\mathcal{F},I}. \tag{49}$$

The distance evaluation between fluid particles and curved polygons requires a high computational cost, and therefore, the polygon walls are approximated as flat triangles in this study even if the original elements are high-order isoparametric elements.

Here, we define a map, NCR, that represents the node correspondence relation between nodes of the polygons and the elements on the fluid–structure interface, $\tilde{L} \in \tilde{\Lambda}_{\text{pnode}}$ and $\tilde{K} \in \tilde{\Lambda}_{\text{fnode}}$, as

$$\tilde{K} = \text{NCR}(\tilde{L}). \tag{50}$$

Since the number of nodes in both the fluid and structure are the same, NCR is a bijective mapping. Therefore, the inverse mapping, NCR^{-1} , exists as

$$\tilde{L} = \text{NCR}^{-1}(\tilde{K}). \tag{51}$$

These node correspondence relation data are necessary for the partitioned coupling analyses conducted in this study.

FSI model from fluid to structure

The EPR model defines the force exerted on the particle i by walls, f_i^{wall} , as

$$f_i^{\text{wall}} = V_i \left(-\langle \nabla p \rangle_i^{\text{ERP}} + \mu \langle \nabla^2 \mathbf{v} \rangle_i^{\text{ERP}} \right). \tag{52}$$

As shown in Fig. 4, we assume that this force is located at the closest point, $\mathbf{x}_i^{\text{wall}}$, defined in Eq. (18), as a point load. The traction force of the fluid can be approximated as

$$\boldsymbol{\sigma}^F \mathbf{n}^F \simeq \sum_{i=1}^{N_{\text{particle}}} \delta(\mathbf{x} - \mathbf{x}_i^{\text{wall}}) f_i^{\text{wall}}, \tag{53}$$

where δ represents the Dirac delta function.

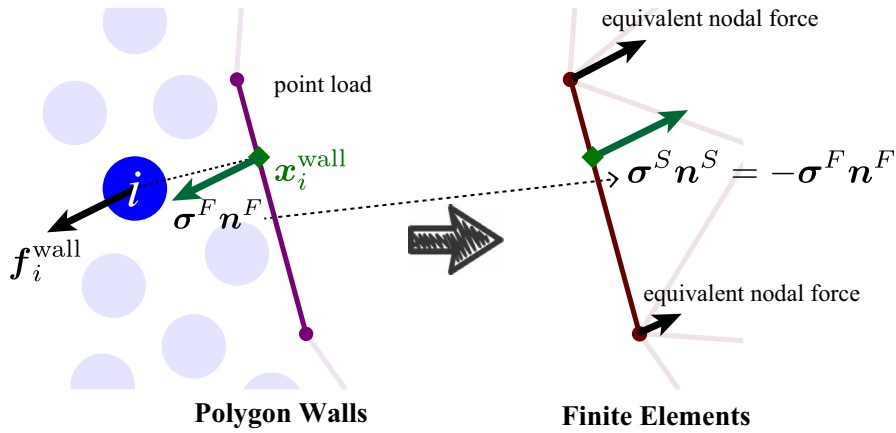


Fig. 4 Point load on polygon wall exerted by particle i and equivalent nodal forces corresponding to the load

The equivalent nodal force exerted from the fluid to the structure at the global node of the polygon wall, \tilde{L} , which corresponds to the second term of right-hand side in Eq. (31), is obtained as

$$\mathbf{f}_{\tilde{L}}^{F \rightarrow S} = \int_{\Gamma_I} \boldsymbol{\sigma}^S \mathbf{n}^S N_{\text{NCR}(\tilde{L})}(\mathbf{x}) d\Gamma. \quad (54)$$

Substituting the force boundary condition on the fluid–structure interface (Eq. (6)) into Eq. (54), the equivalent nodal force can be finally computed as

$$\mathbf{f}_{\tilde{L}}^{F \rightarrow S} = \int_{\Gamma_I} -\boldsymbol{\sigma}^F \mathbf{n}^F N_{\text{NCR}(\tilde{L})}(\mathbf{x}) d\Gamma \quad (55)$$

$$= \int_{\Gamma_I} - \left(\sum_{i=1}^{N_{\text{particle}}} \delta(\mathbf{x} - \mathbf{x}_i^{\text{wall}}) \mathbf{f}_i^{\text{wall}} \right) N_{\text{NCR}(\tilde{L})}(\mathbf{x}) d\Gamma \quad (56)$$

$$= - \sum_{i=1}^{N_{\text{particle}}} \int_{\Gamma_I} \delta(\mathbf{x} - \mathbf{x}_i^{\text{wall}}) \mathbf{f}_i^{\text{wall}} N_{\text{NCR}(\tilde{L})}(\mathbf{x}) d\Gamma, \quad (57)$$

$$= - \sum_{i=1}^{N_{\text{particle}}} \mathbf{f}_i^{\text{wall}} N_{\text{NCR}(\tilde{L})}(\mathbf{x}_i^{\text{wall}}). \quad (58)$$

These forces from the fluid to the structure on each polygon node are projected to the corresponding global node, $\tilde{K} = \text{NCR}(\tilde{L})$, in the FEM as

$$\mathbf{f}_{\text{NCR}(\tilde{L})}^{F \rightarrow S} = \mathbf{f}_{\tilde{L}}^{F \rightarrow S}. \quad (59)$$

FSI model from the structure to the fluid

The contribution from the structure to the fluid can be simply represented by renewing the position, velocity, and acceleration values at the global node of polygon walls \tilde{L} using the displacement, velocity, and acceleration values at the corresponding global node of finite elements, $\tilde{K} = \text{NCR}(\tilde{L})$, obtained by the FEM computation as

$$\mathbf{x}_{\text{NCR}^{-1}(\tilde{K})} = \mathbf{x}_{\tilde{K}}^0 + \mathbf{u}_{\tilde{K}}, \quad (60)$$

$$\mathbf{v}_{\text{NCR}^{-1}(\tilde{K})} = \mathbf{v}_{\tilde{K}}, \tag{61}$$

$$\mathbf{a}_{\text{NCR}^{-1}(\tilde{K})} = \mathbf{a}_{\tilde{K}}. \tag{62}$$

This procedure satisfies the boundary condition of the velocity on the fluid–structure interface given by Eq. (5).

The predictors of the displacement, velocity, and acceleration of polygon walls can be determined based on the known results of structural computations, and they are used as the wall boundary condition in the fluid computation. We adopt the acceleration at a node \tilde{K} in the n th step as the predicted acceleration, $\hat{\mathbf{a}}_{\tilde{K}}^{n+1}$, as

$$\hat{\mathbf{a}}_{\tilde{K}}^{n+1} \simeq \mathbf{a}_{\tilde{K}}^n. \tag{63}$$

Substituting this into the equations of the time integration based on the Newmark’s beta method, Eqs. (40) and (41), the predicted displacement and velocity, $\hat{\mathbf{u}}_{\tilde{K}}^{n+1}$ and $\hat{\mathbf{v}}_{\tilde{K}}^{n+1}$, can be expressed as

$$\hat{\mathbf{u}}_{\tilde{K}}^{n+1}(\Delta t) = \mathbf{u}_{\tilde{K}}^n + \Delta t \mathbf{v}_{\tilde{K}}^n + \frac{1}{2} \Delta t^2 \mathbf{a}_{\tilde{K}}^n, \tag{64}$$

$$\hat{\mathbf{v}}_{\tilde{K}}^{n+1}(\Delta t) = \mathbf{v}_{\tilde{K}}^n + \Delta t \mathbf{a}_{\tilde{K}}^n. \tag{65}$$

Their equations are second-order interpolation for the displacement, and first-order for the velocity from t^n to t^{n+1} .

Partitioned coupling scheme

Partitioned coupling schemes [55,71–73] solve each physical field separately while exchanging information. Although a smaller time step width is often required for sufficient coupling to be achieved in the case of strong interaction problems, partitioned approaches have the advantage of software modularity, which allows the use of existing solvers.

For the fluid and structural computations as abstract functions, \mathcal{F} and \mathcal{S} , respectively, these computations in the partitioned coupled analyses can be written as

$$(\mathbf{v}_\Gamma, p_\Gamma) = \mathcal{F}(\mathbf{x}_\Gamma), \tag{66}$$

$$(\mathbf{x}_\Gamma) = \mathcal{S}(\mathbf{v}_\Gamma, p_\Gamma), \tag{67}$$

where $\mathbf{x}_\Gamma, \mathbf{v}_\Gamma$, and p_Γ represents the position, velocity, and pressure on the fluid–structure interface, Γ_I , respectively. A residual vector whose components are the difference between positions before and after a coupling computation is given as

$$\mathbf{r} = \mathbf{x}_\Gamma - \mathcal{S}(\mathcal{F}(\mathbf{x}_\Gamma)). \tag{68}$$

Partitioned coupling schemes can be categorized into iterative schemes that achieve a strong coupling and staggered schemes (so called weak coupling). In analogy with the iterative methods for linear systems, the iterative schemes adopt an iteration loop within a time step that can be selected to treat the entire problem including the coupling effects

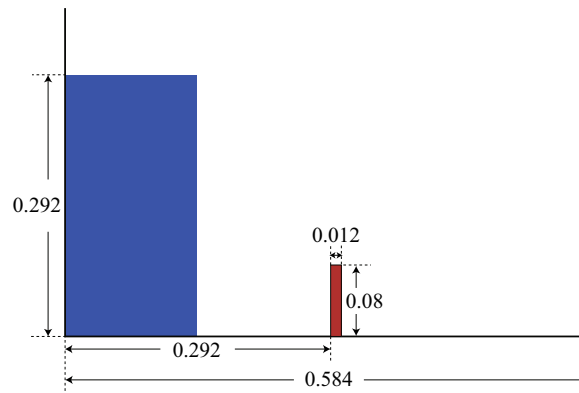


Fig. 5 Dam break problem with an elastic obstacle: initial configuration

Table 2 Dam break with an elastic obstacle: analysis conditions for the fluid computation based on the EMPS method

Time step width	2.5×10^{-6} [s]
Number of particles	20,000 and 80,000
Particle spacing	1.46×10^{-3} and 7.30×10^{-4} [m]
Effective radius	3.1^0 [m]
Density	1.0×10^3 [kg/m ³]
Kinetic viscosity	1.0×10^{-6} [m ² /s]
Gravitational acceleration	10.0[m/s ²]
Sound speed coefficient	17.1[m/s]
Repulsive coefficient in the ERP model	1.0×10^7 [N/m ³]

implicitly. They skip the iteration loop if the L2 norm of the residual vector in the i th iteration is less than a small constant ϵ .

$$\frac{\|r^i\|}{\|r^0\|} < \epsilon (\simeq 0). \tag{69}$$

Thus far, various iterative partitioned schemes have been proposed; for example, the block Gauss–Seidel method [74], block Newton method [72,73], and Broyden method [75]. Staggered schemes such as the conventional parallel staggered scheme, CSS scheme, and improved serial staggered scheme [55] skip the iteration in a coupling step that ignores the norm of the residual.

Verification and validation

Dam break with an elastic obstacle

The dam break problem with an elastic obstacle is solved to verify the proposed FSI model. This problem was initially proposed in a previous study [76] using the space-time FEM, and it has been investigated in other studies [26,33,47,77] for verification.

Figure 5 illustrates the initial configuration of the dam break problem with an elastic obstacle. The elastic obstacle is a linear elastic body that has a width of 0.012[m] and a height of 0.08[m] with a bottom constraint. The water column is 0.146[m] wide and 0.292[m] high. The details of the analysis conditions for the fluid and structure are presented respectively in Tables 2 and 3.

Table 3 Dam break with an elastic obstacle: analysis conditions for structural computation based on the FEM

Time step width	2.5×10^{-6} [s]
Number of elements	48
Element type	Isoparametric 2nd-order
Young's modulus	1.0×10^6 [kg/s ² m]
Poisson's ratio	0.0
Density	2.5×10^3 [kg/m ³]
Gravitational acceleration	10.0[m/s ²]

Table 4 Dam break with an elastic obstacle: details of existing studies

	Fluid	Structure	Coupling type
Ryzhakov et al. [26]	Particle FEM	FEM	Monolithic scheme
Walhorn et al. [76]	Stabilized space-time FEM	Space-time FEM	Monolithic scheme
Idelsohn et al. [77]	Particle FEM	FEM	Monolithic scheme
Rafiee et al. [33]	SPH method	SPH method	Staggered partitioned scheme
Li et al. [47]	SPH-ALE method	FEM	Staggered partitioned scheme

Figure 6 shows the displacement of the upper-left corner of the elastic obstacle obtained in existing studies [26,33,47,76,77]; the numerical methods for fluid and structure, and the coupling type used in their studies are presented in Table 4. As shown in the figure, the qualitative behaviors are similar. The elastic obstacle is deformed to the left a little by the fluid hitting the lower part of the obstacle at approximately $t = 0.15$ [s]. The obstacle deflects to the right because of the force from the fluid, and it reaches the maximum deflection at approximately $t = 0.25$ [s]. In terms of the maximum deflection, the existing studies have a range from 0.04[m] to 0.05[m]. Then, the deflected obstacle pushes the fluid back while the fluid climbs over the obstacle, and then, the results of the existing studies become different. The existing studies based on mesh-based methods for both fluid and structure; Ryzhakov et al. [26], Walhorn et al. [76], and Idelsohn et al. [77]; exhibit relatively similar trends, although studies in which mesh-free particle methods are used for fluid; Rafiee et al. [33] and Li et al. [47] show relatively larger deflections.

The results obtained by the proposed wave-structure model are shown in Figs. 7, 8, and 9; they are similar to the ones in the Ryzhakov's study [26]. Therefore, we compare our results with that in the following discussion.

Figure 7 shows the deflection of the upper-left corner of the obstacle, as in Fig. 6, obtained by the proposed model based on the CSS without predictor. Cases with two spatial resolutions for the fluid computations, 20,000 and 80,000 fluid particles, are compared. Figure 8 shows the deflection obtained by the proposed FSI model based on the CSS with the 2nd-order predictor, which is given by Eqs. (64) and (65). Both the results with and without predictor are like the Ryzhakov's result though the peaks are slightly higher than that. There are a few differences when the spatial resolution is increased in terms of the maximum deflections; the results of the proposed model exhibit small fluctuations from $t = 0.5$ [s] to 0.6[s]. This is caused by a collision of a splash of fluid to the obstacle after the fluid impacts the right wall; this may be very sensitive to the free-surface and wall boundary treatment.

Figure 9 shows the deflection obtained by the proposed FSI model based on the block Gauss-Seidel method in cases with 20,000 and 80,000 fluid particles. The snapshots of the

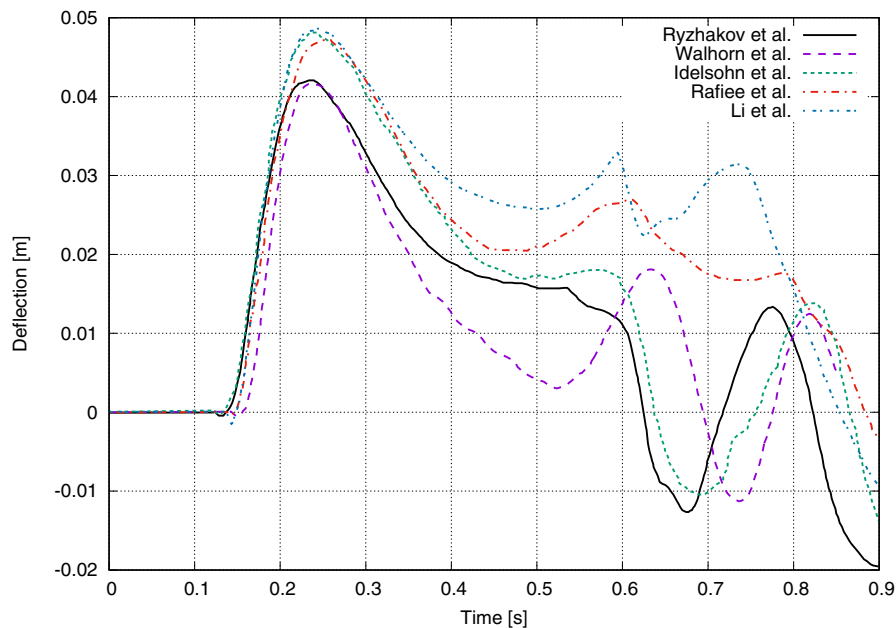


Fig. 6 Dam break with an elastic obstacle: deflection of the upper-left corner of the obstacle obtained in existing studies ([26], [76], [77], [33], and [47])

case with 80,000 particles are shown in Fig. 11. The convergence criterion for the iteration in Eq. (69) is set as $\epsilon = 1.0 \times 10^{-4}$. A Strong coupling in this case is like the nonlinear solver for the boundary nonlinearity of the surfaces of the structure. Although higher accuracy and stability is expected by adopting the iteration, there are slight differences between the cases with the block Gauss–Seidel (BGS) method and CSS. The result indicate that this problem may not have a large coupling effect, and the time step width is sufficiently small for weak coupling because that used for this computation is limited by the fluid computation with the fully explicit algorithm.

Figure 10 shows the number of iterations averaged every 200 steps in the simulation with the BGS method. We limit the number of iterations to 200; there are 200,000 steps in this simulation. Although the number of iterations is less than 10 in most steps, 210 out of all calculation steps do not reach our convergence criteria, and a rapid increase in the number of iterations is observed between $t = 0.45$ [s] to 0.6 [s]. This result coincides with the small fluctuation shown in Figs. 7 and 8, and it is believed to be associated with the isolated droplets of the free-surface particles colliding with the obstacle. In such scenarios, the repulsive force can be dominant, and the initial residual norm can be very small, and this can result in poor convergence properties.

Sloshing tank with an elastic beam

Iglesias et al. [78,79] performed a series of experiments to simulate the free-surface flow interacting with deformable structures as a SPHERIC benchmark test case [80]. Further, they showed the results of the simulations based on PFEM [79]. Yang et al. [49] computed one of the experiments using SPH for free-surface flow and FEM for structure.

Figure 12 illustrates the geometric specifications of the experiment. The length, height, and width of the tank are 0.609 [m], 0.3445 [m], and 0.039 [m], respectively. An elastic beam

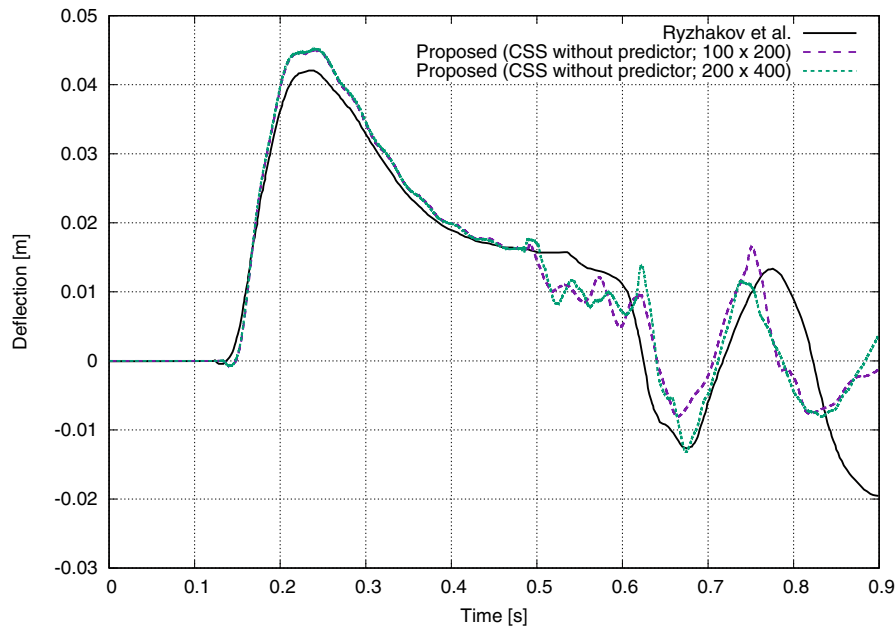


Fig. 7 Dam break with an elastic obstacle: deflection of the upper-left corner of the obstacle obtained by the proposed model based on the conventional serial staggered (CSS) scheme without a predictor

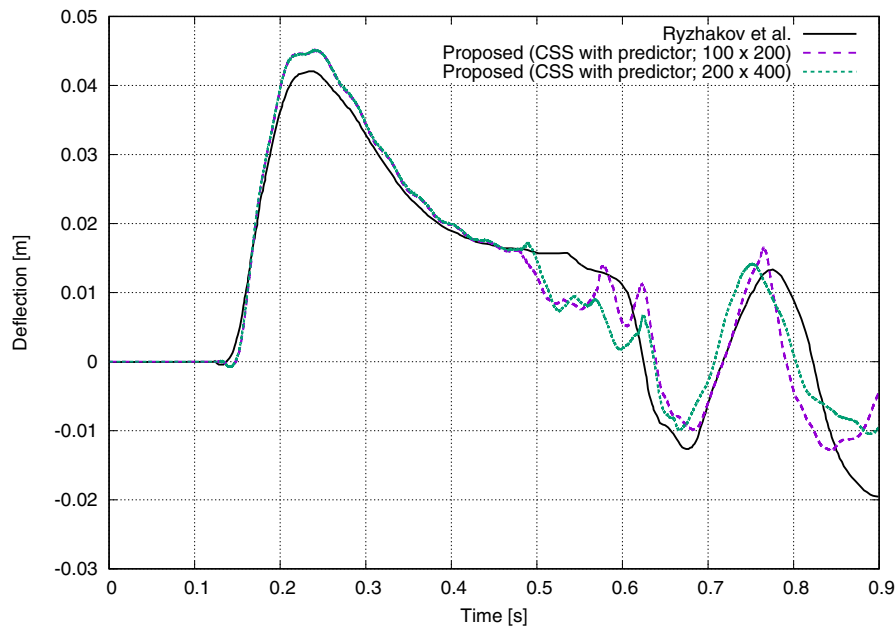


Fig. 8 Dam break with an elastic obstacle: deflection of the upper-left corner of the obstacle obtained by the proposed model based on the conventional serial staggered (CSS) scheme with a second-order predictor

is initially located at the center of the tank, and it is immersed in sunflower oil. There are gaps of 0.0029[m] between the beam and the tank. The tank moves in an oscillatory manner around the center point at the bottom, as shown in Fig. 13. A local coordinate system moving along the tank is defined, and deflection at the top of the beam is measured in the local coordinate system. Figure 14 shows the time history of the roll angle provided in the SPHERIC benchmark website [80].

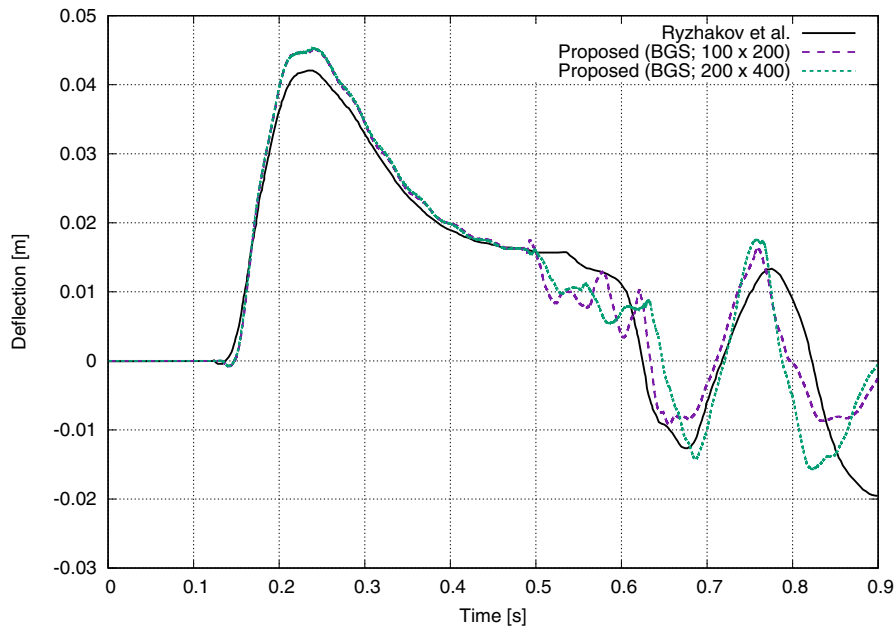


Fig. 9 Dam break with an elastic obstacle: deflection of the upper-left corner of the obstacle obtained by the proposed model based on the block Gauss–Seidel (BGS) method

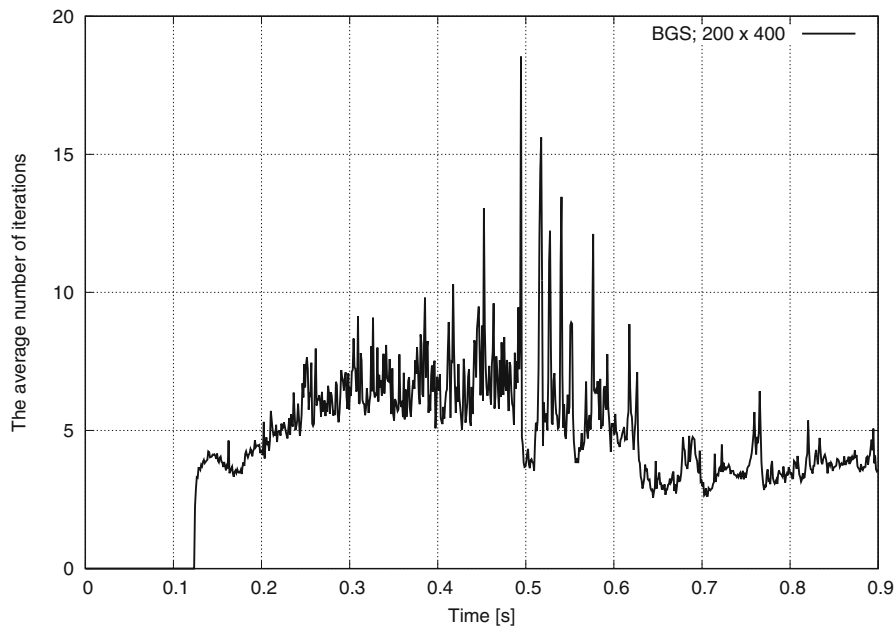


Fig. 10 Dam break with an elastic obstacle: number of iterations in the simulation of the proposed FSI model averaged every 200 steps in the case with the iterative coupling scheme

We conduct two-dimensional simulations of the proposed FSI model to reproduce the experiment with the initial configuration shown in Fig. 12 and we use the roll angle shown in Fig. 14. Tables 5 and 6 present the analysis conditions for the fluid and structural computations. Further, we use the same physical values of the oil and the beam (density, kinetic viscosity, and Young’s ratio) as that provided in the report [80].

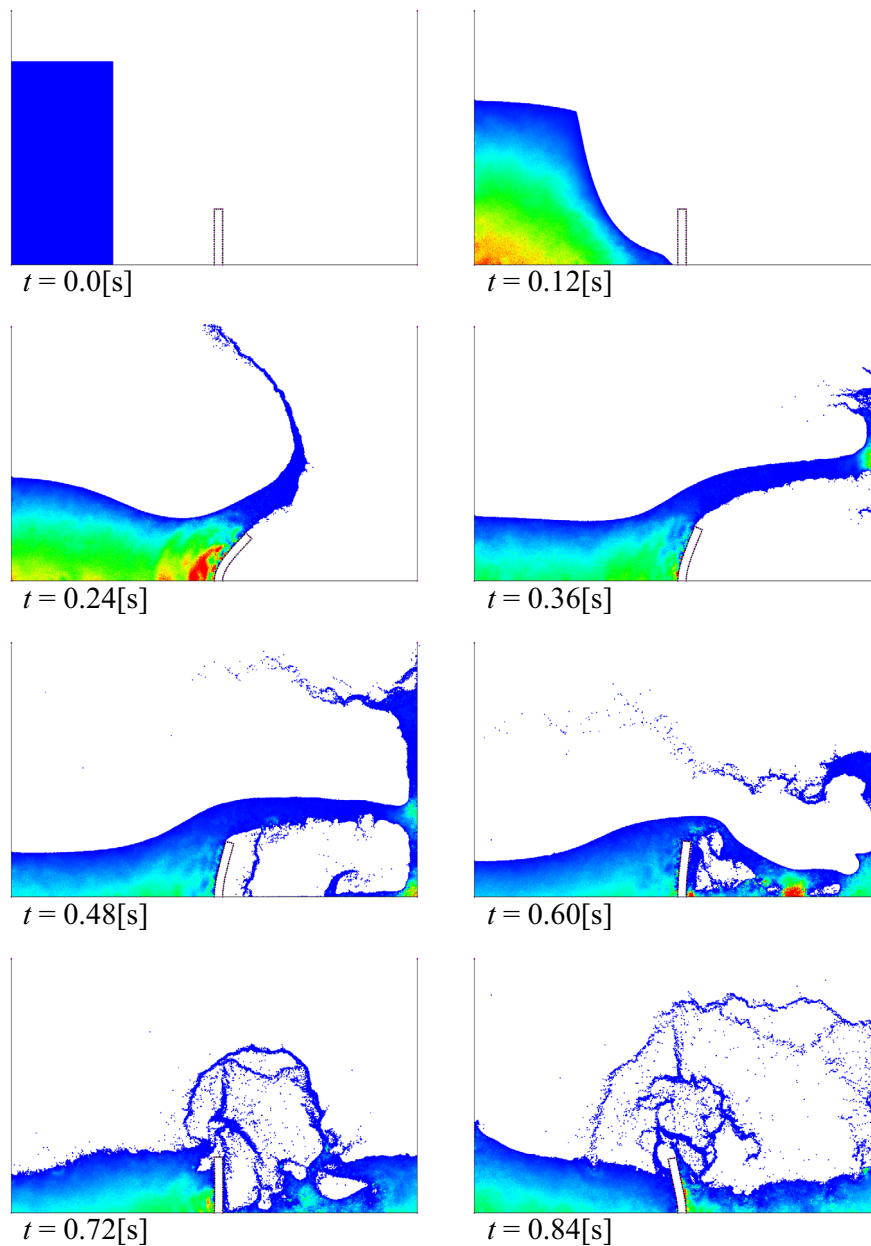


Fig. 11 Dam break with an elastic obstacle: snapshots of the simulation conducted by the proposed model based on the block Gauss–Seidel (BGS) method from $t = 0.0[s]$ to $t = 0.84[s]$; pressure contours are indicated by color (min: $0.0[N/m^2]$, max: $2500.0[N/m^2]$)

In the following considerations, we use the result in the case with a time spacing of $1.0 \times 10^{-4}[s]$, initial particle spacing of $2.5 \times 10^{-3}[m]$, predictor, and CSS scheme.

Figure 15 shows the displacement in the x direction at the top of the beam observed in the local coordinate system as computed by the proposed FSI model. The result is compared with that of the experiment, and with the two-dimensional numerical results of the PFEM (Souto-Iglesias et al. [79]) and SPH-FEM (Yang et al. [49]). The PFEM computation is conducted from $0.0[s]$ to $5.0[s]$. Although the result of the proposed model overestimates

Table 5 Sloshing tank with an elastic beam: analysis conditions for the fluid computation

Time step width	1.0×10^{-4} and 5.0×10^{-5} [s]
Number of particles	44,528 and 278,300
Particle spacing	2.5×10^{-3} and 5.0×10^{-4} [m]
Effective radius	$3.1l^0$ [m]
Density	9.0×10^2 [kg/m ³]
Kinetic viscosity	5.0×10^{-5} [m ² /s]
Gravitational acceleration	9.81[m/s ²]
Sound speed coefficient	10.59[m/s]
Repulsive coefficient in the ERP model	1.0×10^7 [N/m ³]

Table 6 Sloshing tank with an elastic beam: analysis conditions for the structural computation

Time step width	1.0×10^{-4} and 5.0×10^{-5} [s]
Number of elements	200
Element type	Isoparametric 2nd-order
Young's modulus	3.3×10^6 [kg/s ² m]
Poisson's ratio	0.49
Density	1.1×10^3 [kg/m ³]
Gravitational acceleration	9.81[m/s ²]

the peak displacements, it agrees well with the result of the PFEM. We will discuss the overestimation later.

We conduct sensitivity tests in terms of the effect of the predictor, time spacing, and spatial resolution. Figure 16 shows the results with and without the predictor, and Fig. 17 shows the ones with $\Delta t = 1.0 \times 10^{-4}$ [s] and 5.0×10^{-5} [s]. There are almost no difference between the results, and therefore, in this test case, these effects can be considered trivial. Figure 18 shows the difference between the cases with $l^0 = 2.5 \times 10^{-3}$ [m] (44,528 fluid particles) and $l^0 = 5.0 \times 10^{-4}$ [m] (278,300 fluid particles). The peak displacements in the higher spatial resolution are slightly small compared with those of the coarser ones.

Figure 19 shows the results obtained using the proposed FSI model with the CSS coupling and iterative partitioned coupling scheme with the BGS method. The number of iterations averaged every 100 steps in the case with the BGS method is presented in Fig. 20. We set the small constant used as a convergence criterion in equation (69) to 1.0×10^{-4} . The snapshots of that simulation are presented in Fig. 21. The result with the BGS method exhibits smaller peak displacements compared to that with the CSS scheme. A comparison of the second positive peak displacement of the numerical results of the proposed model with the experiment results indicates differences of about 13.0% in the case with the BGS method and 25.3% with the CSS scheme. Though the result provided by Yang et al. are in good agreement with the experiment results, as indicated in Fig. 15, the overestimations seen in the results obtained by the proposed model and the PFEM seem reasonable. This is because the experimental setting has gaps of 0.0029[m] between the tank and the beam, as illustrated in Fig. 12. The area without the gaps is approximately 14.9% larger than the one with the gaps. Focusing on the pressure difference between the left and right regions, displacement of the structure is proportional to surface area in the case of a linear elastic body. Although it is difficult to discuss rigorously because of the nonlinear deformation, overestimations can occur because two-dimensional simulations implicitly assume no gap. In addition, the two-dimensional simulations do not have

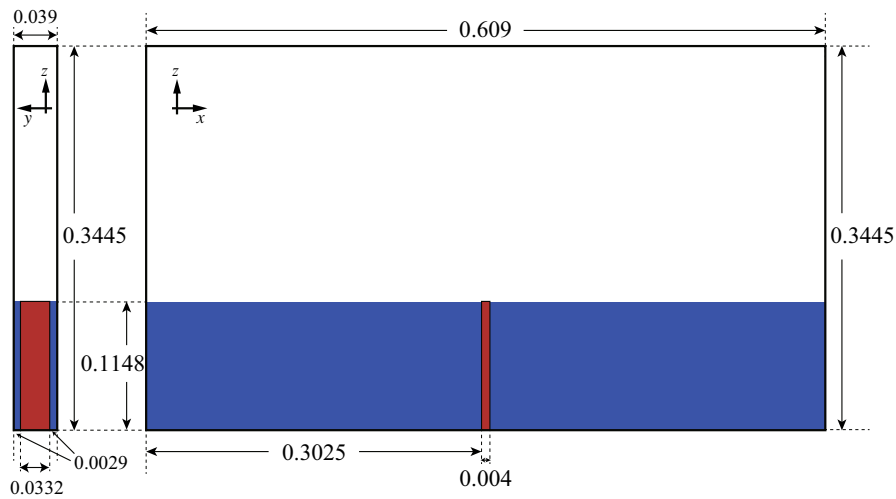


Fig. 12 Slicing tank with an elastic beam: initial configuration

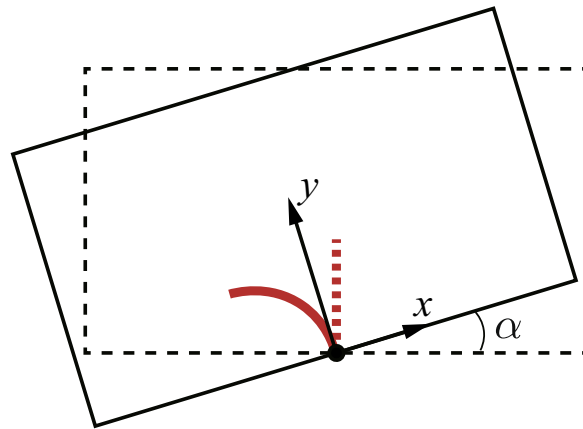


Fig. 13 Slicing tank with an elastic beam: coordinate system for the tank

fluid flowing in and out between the left and right regions through the gap compared to the experiment. Therefore, the water level difference is expected to be more pronounced than in the experiment, and the pressure difference due to the water level difference is also expected to peak later. The displacement of the elastic body is expected to follow this peak. It also contributes to overestimations of displacement in two-dimensional simulations and is thought to be the cause of the phase difference from the experimental values as seen in Fig. 19. However, there are also three-dimensional effects or dynamic pressures caused by flow through the gaps; these three-dimensional computations should be conducted as part of a future work for further discussion of this test case.

Conclusions

This study presented a compatible interface wave–structure interaction model based on a mesh-free particle method for free-surface flow analysis, and the FEM for structural analysis.

The EMPS method is employed for free-surface flow analysis. We adopted the ERP wall boundary model [56] in the EMPS method. The proposed model was geometrically

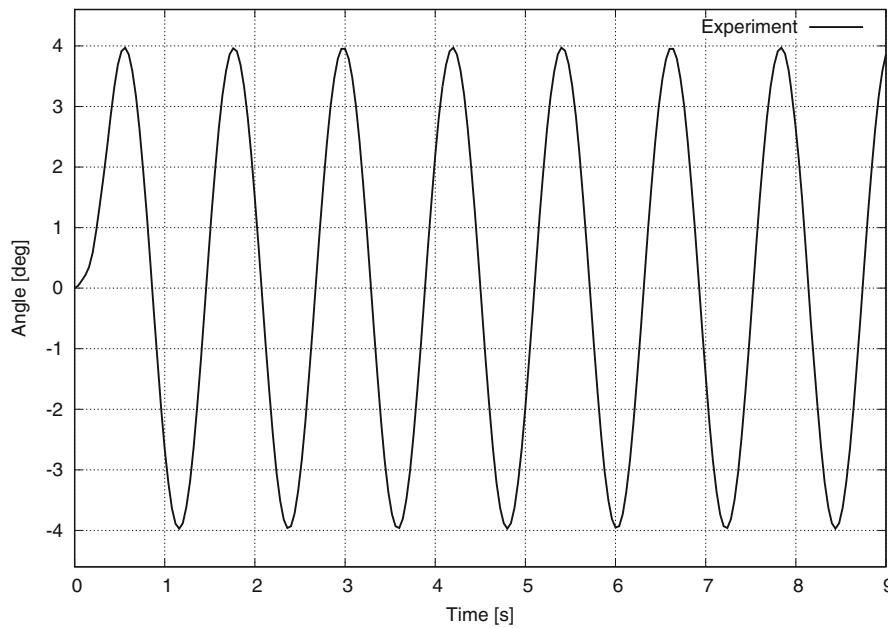


Fig. 14 Sloshing tank with an elastic beam: roll angle in the experiment

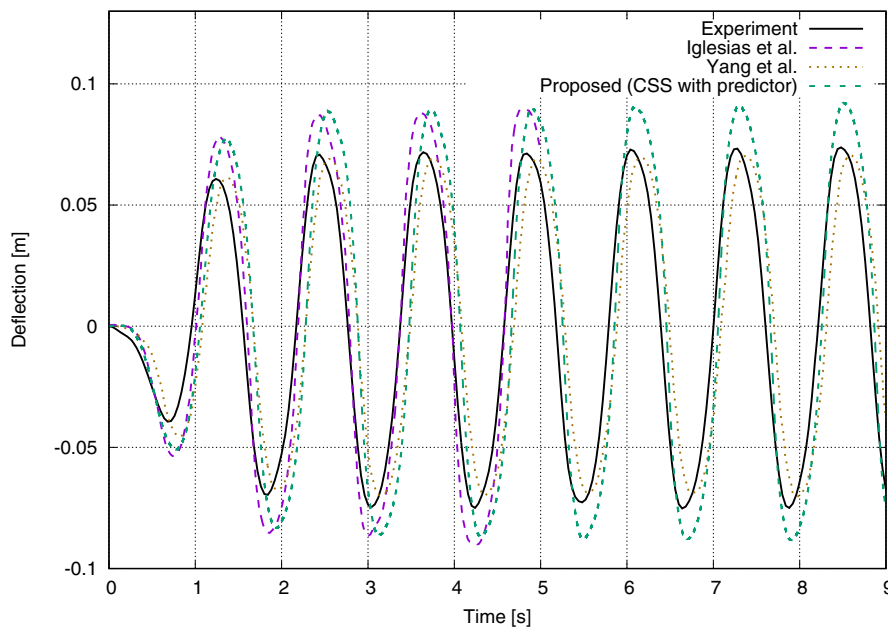


Fig. 15 Sloshing tank with an elastic beam: displacements of the x direction at the top of the beam obtained by the proposed FSI model compared to experiments and numerical results in the existing studies ([79] and [49])

compatible on the interfaces because the ERP model could directly use FE surfaces and their shape functions on fluid–structure interfaces.

The force exerted by fluid particles on structures was modeled as point loads using the Dirac delta function based on the compatible interface between the polygons and the finite elements. This procedure was relatively simple and satisfied the kinetic boundary condition on the fluid–structure interface. We formulated a predictor for the displacement and velocity to verify its effectiveness when used with the staggered (weak coupling)

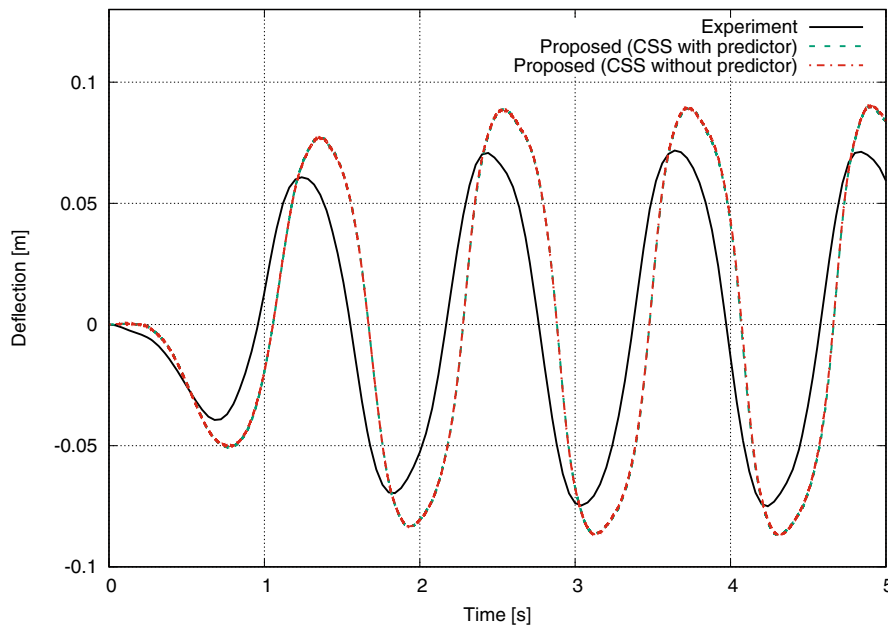


Fig. 16 Sloshing tank with an elastic beam: displacements of the x direction at the top of the beam obtained by the proposed FSI model with and without the second-order predictor

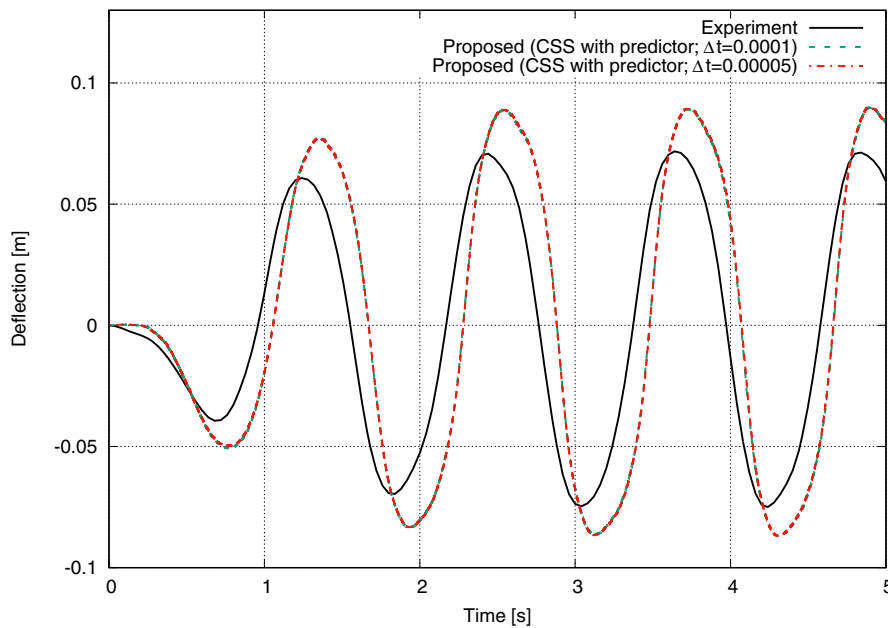


Fig. 17 Sloshing tank with an elastic beam: displacements of the x direction at the top of the beam obtained by the proposed FSI model with different time spacings

schemes. Further, we developed a strong coupling algorithm based on an iterative partitioned scheme with the BGS method.

We performed verification and validation tests and sensitivity tests for the effect of the predictor, time spacing, and spatial resolution by solving two benchmark problems. The results obtained for the dam break problem with an elastic obstacle using the proposed wave–structure model exhibited good agreement with the ones reported in Ryzhakov’s

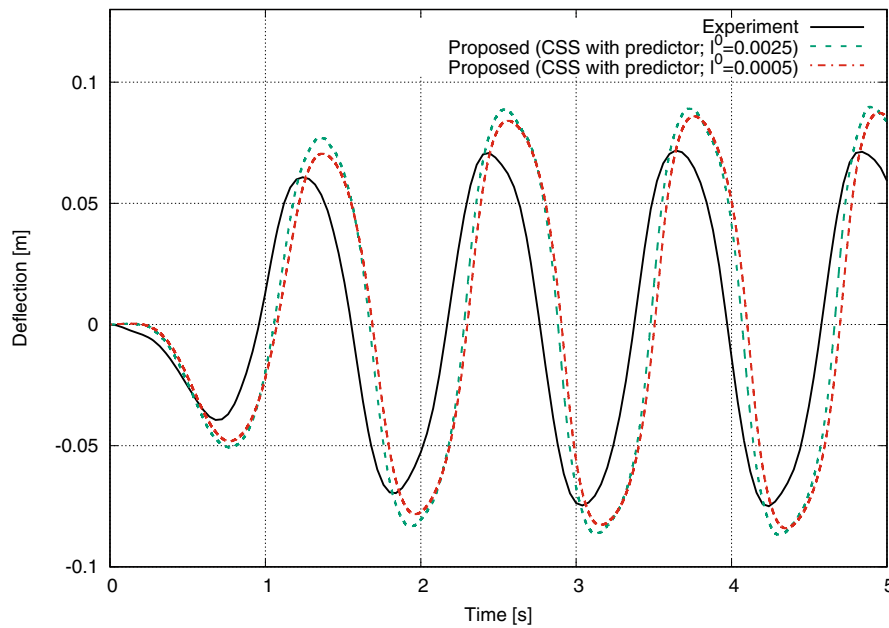


Fig. 18 Sloshing tank with an elastic beam: displacements of x direction at the top of the beam obtained by the proposed FSI model with different spatial resolutions

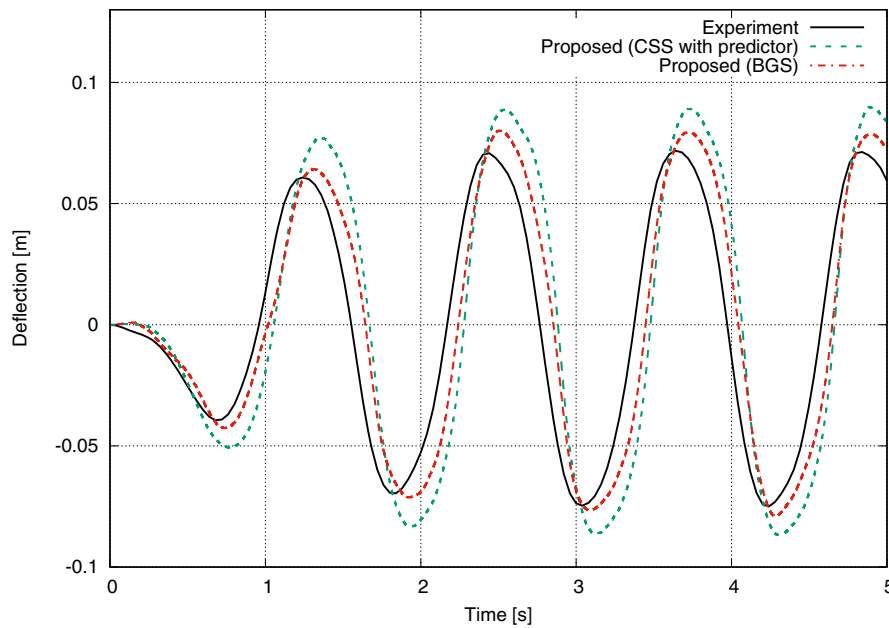


Fig. 19 Sloshing tank with an elastic beam: displacements of the x direction at the top of the beam obtained by the proposed FSI model with the CSS scheme and iterative coupling scheme based on the block Gauss–Seidel (BGS) method

study [26], which adopts a strong coupling scheme and the particle FEM. In this test case, there are little difference in the cases with the BGS method (strong coupling) and CSS method (weak coupling). The result indicate that this problem may not have a large coupling effect, and the time step width is sufficiently small for weak coupling because the time step width used for this computation is limited by the fluid computation with

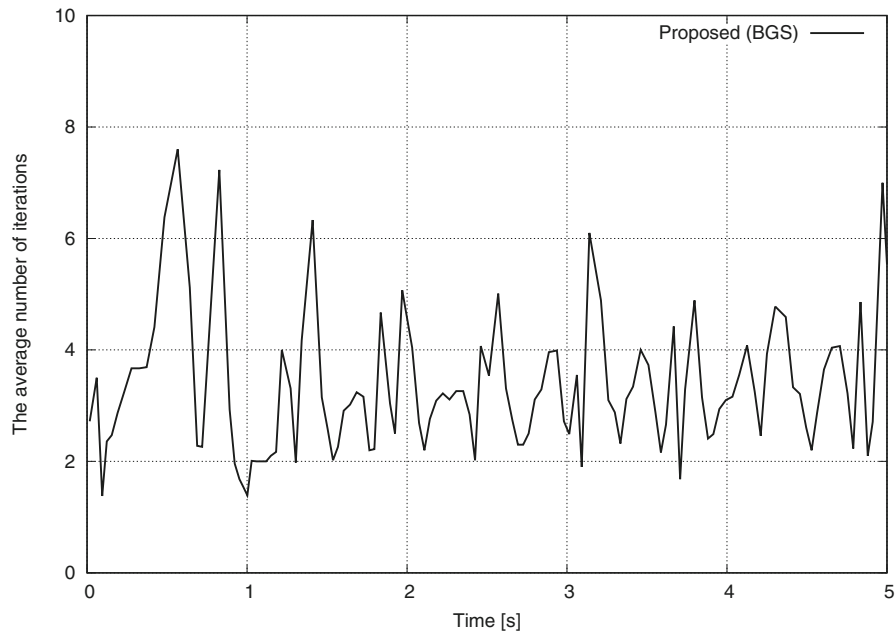


Fig. 20 Sloshing tank with an elastic beam: number of iterations in the simulation of the proposed FSI model averaged every 100 steps in the case with the iterative coupling scheme

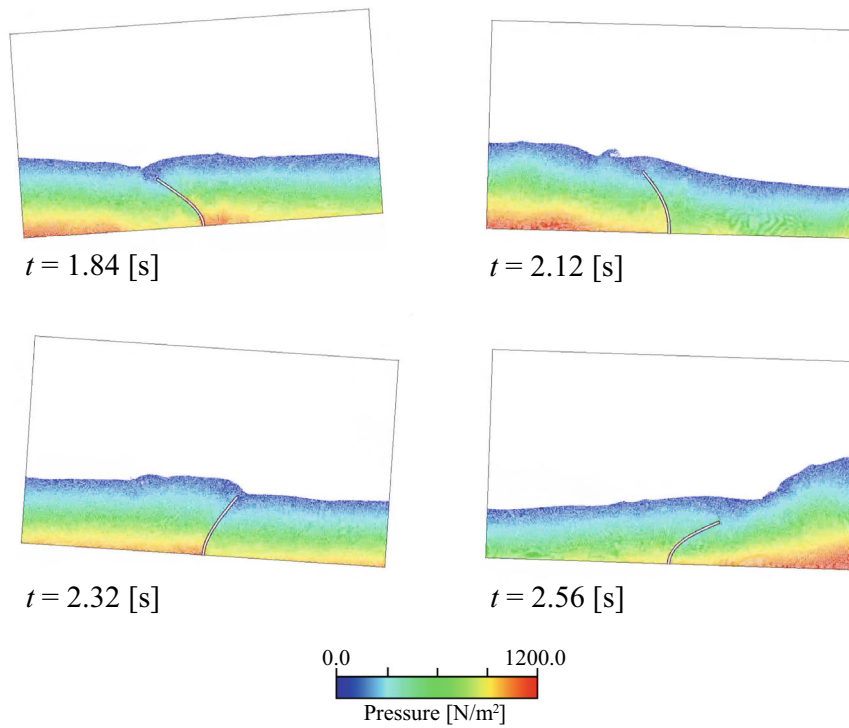


Fig. 21 Sloshing tank with an elastic beam: snapshots of the simulation conducted by the proposed model based on the block Gauss–Seidel method at $t = 1.84, 2.12, 2.32,$ and $2.56[s]$; pressure contours are indicated by color (min: $0.0[N/m^2]$, max: $1200.0[N/m^2]$)

the fully explicit algorithm. However, this result is valuable because we cannot discuss the coupling effect without attempting the strong coupling scheme. Next, we simulated an experiment of a sloshing tank with an elastic beam. Although the results of the proposed model overestimated the peak displacements compared with those of the experiment, it agreed well with the result of the existing study that uses particle FEM (Souto-Iglesias et al. [79]). The experimental setting has gaps between the tank and the beam. This study conducted two-dimensional simulations, which implicitly assumed no gap, and therefore, overestimations were considered to occur.

Incorporating the three-dimensional and parallel simulator for the EMPS method and ERP wall boundary model [59] to achieve three-dimensional wave–structure interaction analysis will be considered as a future task for practical applications. The 3D simulator would also allow for a more quantitative discussion of the issues in “[Sloshing tank with an elastic beam](#)”.

Acknowledgements

This work was supported by a JSPS Grant-in-Aid for Scientific Research (B) (Grant Number 22H03601) and JST FOREST Program (Grant Number JPMJFR215S).

Author contributions

NM developed the proposed model in this study. NM conducted the verification and validation test cases and interpreted the results. NM wrote this manuscript.

Funding

Japan Society for the Promotion of Science, Grant-in-Aid for Scientific Research (B), 22H03601. Japan Science and the Technology Agency, Fusion Oriented REsearch for disruptive Science and Technology (FOREST), JPMJFR215S.

Availability of data and materials

The datasets used and/or analysed during the current study are available from the corresponding author on reasonable request.

Declarations

Competing interests

They have no competing interests.

Received: 1 December 2022 Accepted: 28 May 2023

Published online: 26 July 2023

References

1. Asakura R, Iwase K, Ikeya T, Takao M, Kaneto T, Fujii N. et al. Experimental study on wave force acting on on-shore structures due to overflowing tsunamis. In: *Proceedings of Coastal Engineering*. vol. 47. Japan Society of Civil Engineers; 2000. p. 911–915. **(in Japanese)**.
2. Asakura R, Iwase K, Ikeya T, Takao M, Kaneto T, Fujii N. et al. The tsunami wave force acting on land structures. In: *Proceedings of 28th International Conference on Coastal Engineering*; 2002. p. 1191–1202.
3. Ikeno M, Matsuyama M, Tanaka H. Shoaling and soliton fission of tsunami on a shelf and wave pressure for tsunami-resistant design of breakwater by large wave flume-experiments. In: *Proceedings of Coastal Engineering*. vol. 45; 1998. p. 366–370. **(in Japanese)**.
4. Ikeno M, Mori N, Tanaka H. Experimental study on drift behavior and its impulse force by tsunami. *Annual J Coast Eng*. 2001;48:846–50 **(in Japanese)**.
5. Matsutomi H. A practical formula for estimating impulsive force due to driftwoods and variation features of the impulsive forces. *J Hydraulic Coast Environ Eng*. 1999;621:111–27 **(in Japanese)**.
6. Grilli ST, Harris JC, Bakhsh TST, Masterlark TL, Kyriakopoulos C, Kirby JT, et al. Numerical simulation of the 2011 Tohoku tsunami based on a new transient FEM co-seismic source: comparison to far-and near-field observations. *Pure Appl Geophys*. 2013;170(6–8):1333–59.
7. Oishi Y, Imamura F, Sugawara D. Near-field tsunami inundation forecast using the parallel TUNAMI-N2 model: application to the 2011 Tohoku-Oki earthquake combined with source inversions. *Geophys Res Lett*. 2015;42(4):1083–91.
8. Westerink JJ, Luettich RA, Feyen JC, Atkinson JH, Dawson C, Roberts HJ, et al. A basin-to channel-scale unstructured grid hurricane storm surge model applied to southern Louisiana. *Mon Weather Rev*. 2008;136(3):833–64.
9. Dao M, Tkalich P. Tsunami propagation modelling? A sensitivity study. *Natural Hazards Earth Syst Sci*. 2007;7(6):741–54.
10. Hamzah MA, Mase H, Takayama T. Simulation and experiment of hydrodynamic pressure on a tsunami barrier. In: *Proceedings of Coastal Engineering*. vol. 47; 2000. p. 371–375 **(in Japanese)**.

11. Murotani K, Koshizuka S, Tamai T, Shibata K, Mitsume N, Shinobu Y, et al. Development of hierarchical domain decomposition explicit MPS method and application to large-scale tsunami analysis with floating objects. *J Adv Simul Sci Eng*. 2014;1(1):16–35.
12. Yoneyama N, Nagashima H. Development of a three dimensional numerical analysis method for the drift behavior in tsunami. *J Jpn Soc Civil Eng Ser B2 (Coast Eng)*. 2009;65(1):266–70.
13. Pringle WJ, Yoneyama N, Mori N. Two-way coupled long wave-RANS model: solitary wave transformation and breaking on a plane beach. *Coast Eng*. 2016;114:99–118.
14. Sitanggang K, Lynett P. Multi-scale simulation with a hybrid Boussinesq-RANS hydrodynamic model. *Int J Numer Meth Fluids*. 2010;62(9):1013–46.
15. Takase S, Moriguchi S, Terada K, Kato J, Kyoya T, Kashiya K, et al. 2D–3D hybrid stabilized finite element method for tsunami runup simulations. *Comput Mech*. 2016;58(3):411–22.
16. Mitsume N, Donahue AS, Westerink JJ, Yoshimura S. Coupling methods between finite element-based Boussinesq-type wave and particle-based free-surface flow models. *Int J Numer Meth Fluids*. 2018;88(3):141–68.
17. Sato S, Okayasu A, Yeh H, Fritz HM, Tajima Y, Shimozono T. Delayed survey of the 2011 Tohoku Tsunami in the former exclusion zone in Minami-Soma, Fukushima Prefecture. *Pure Appl Geophys*. 2014;171(12):3229–40.
18. Yoshimura S, Nakamura H, Kanayama H, Aoki T, Himeno T, Sakai Y, et al. Understanding the mechanism of tsunami-induced damage to machines and structures based on a discipline of mechanics. In: Report of the JSME Research Committee on the Great East Japan Earthquake Disaster. The Japan Society of Mechanical Engineers; 2014; p. 24–57.
19. Hirt CW, Nichols BD. Volume of fluid (VOF) method for the dynamics of free boundaries. *J Comput Phys*. 1981;39(1):201–25.
20. Fedkiw SOR. Level set methods and dynamic implicit surfaces. 2003.
21. Osher S, Sethian JA. Fronts propagating with curvature-dependent speed: algorithms based on Hamilton-Jacobi formulations. *J Comput Phys*. 1988;79(1):12–49.
22. Idelsohn S, Oñate E, Pin FD, Calvo N. Fluid-structure interaction using the particle finite element method. *Comput Methods Appl Mech Eng*. 2006;195(17):2100–23.
23. Idelsohn SR, Oñate E, Pin FD. The particle finite element method: a powerful tool to solve incompressible flows with free-surfaces and breaking waves. *Int J Numer Meth Eng*. 2004;61(7):964–89.
24. Oñate E, Celigueta MA, Idelsohn SR, Salazar F, Suárez B. Possibilities of the particle finite element method for fluid-soil-structure interaction problems. *Comput Mech*. 2011;48(3):307–18.
25. Oñate E, Idelsohn SR, Del Pin F, Aubry R. The particle finite element method—an overview. *Int J Comput Methods*. 2004;1(02):267–307.
26. Ryzhakov P, Rossi R, Idelsohn S, Oñate E. A monolithic Lagrangian approach for fluid–structure interaction problems. *Comput Mech*. 2010;46(6):883–99.
27. Gingold RA, Monaghan JJ. Smoothed particle hydrodynamics: theory and application to non-spherical stars. *Mon Not R Astron Soc*. 1977;181(3):375–89.
28. Lucy LB. A numerical approach to the testing of the fission hypothesis. *Astron J*. 1977;82:1013–24.
29. Koshizuka S, Oka Y. Moving-particle semi-implicit method for fragmentation of incompressible fluid. *Nucl Sci Eng*. 1996;123(3):421–34.
30. Antoci C, Gallati M, Sibilla S. Numerical simulation of fluid–structure interaction by SPH. *Comput Struct*. 2007;85(11):879–90.
31. Chikazawa Y, Koshizuka S, Oka Y. A particle method for elastic and visco-plastic structures and fluid–structure interactions. *Comput Mech*. 2001;27(2):97–106.
32. Hwang SC, Khayyer A, Gotoh H, Park JC. Development of a fully Lagrangian MPS-based coupled method for simulation of fluid–structure interaction problems. *J Fluids Struct*. 2014;50:497–511.
33. Rafiee A, Thiagarajan KP. An SPH projection method for simulating fluid-hypoelastic structure interaction. *Comput Methods Appl Mech Eng*. 2009;198(33):2785–95.
34. Aktay L, Johnson AF. FEM/SPH coupling technique for high velocity impact simulations. In: *Advances in Meshfree Techniques*. Springer; 2007; p. 147–167.
35. Attaway SW, Heinstein MW, Swegle JW. Coupling of smooth particle hydrodynamics with the finite element method. *Nucl Eng Des*. 1994;150(2):199–205.
36. De Vuyst T, Vignjevic R, Campbell J. Coupling between meshless and finite element methods. *Int J Impact Eng*. 2005;31(8):1054–64.
37. Gu Y, Zhang L. Coupling of the meshfree and finite element methods for determination of the crack tip fields. *Eng Fract Mech*. 2008;75(5):986–1004.
38. Johnson GR. Linking of Lagrangian particle methods to standard finite element methods for high velocity impact computations. *Nucl Eng Des*. 1994;150(2):265–74.
39. Lu Y, Wang Z, Chong K. A comparative study of buried structure in soil subjected to blast load using 2D and 3D numerical simulations. *Soil Dyn Earthq Eng*. 2005;25(4):275–88.
40. Anghileri M, Castelletti LM, Tirelli M. Fluid–structure interaction of water filled tanks during the impact with the ground. *Int J Impact Eng*. 2005;31(3):235–54.
41. Comas-Cardona S, Groenenboom P, Binetruy C, Krawczak P. A generic mixed FE-SPH method to address hydro-mechanical coupling in liquid composite moulding processes. *Compos A Appl Sci Manuf*. 2005;36(7):1004–10.
42. Fourey G, Oger G, Le Touzé D, Alessandrini B. violent fluid–structure interaction simulations using a coupled SPH/FEM method. In: *IOP Conference Series: Materials Science and Engineering*. vol. 10. IOP Publishing; 2010; p. 012041.
43. Groenenboom PH, Cartwright BK. Hydrodynamics and fluid–structure interaction by coupled SPH-FE method. *J Hydraul Res*. 2010;48(S1):61–73.
44. Hu D, Long T, Xiao Y, Han X, Gu Y. Fluid–structure interaction analysis by coupled FE-SPH model based on a novel searching algorithm. *Comput Methods Appl Mech Eng*. 2014;276:266–86.
45. Lee CJK, Noguchi H, Koshizuka S. Fluid–shell structure interaction analysis by coupled particle and finite element method. *Comput Struct*. 2007;85(11):688–97.

46. Li Z, Leduc J, Combescure A, Leboeuf F. Coupling of SPH-ALE method and finite element method for transient fluid–structure interaction. *Comput Fluids*. 2014;103:6–17.
47. Li Z, Leduc J, Nunez-Ramirez J, Combescure A, Marongiu JC. A non-intrusive partitioned approach to couple smoothed particle hydrodynamics and finite element methods for transient fluid-structure interaction problems with large interface motion. *Comput Mech*. 2015; 1–22.
48. Thiyahuddin M, Gu Y, Gover R, Thambiratnam D. Fluid–structure interaction analysis of full scale vehicle-barrier impact using coupled SPH-FEA. *Eng Anal Boundary Elem*. 2014;42:26–36.
49. Yang Q, Jones V, McCue L. Free-surface flow interactions with deformable structures using an SPH-FEM model. *Ocean Eng*. 2012;2012(55):136–47.
50. Yang Q. SPH Simulation of fluid–structure interaction problems with application to hovercraft. Virginia Polytechnic Institute and State University; 2012;
51. Vila J. On particle weighted methods and smooth particle hydrodynamics. *Math Models Methods Appl Sci*. 1999;9(02):161–209.
52. Mitsume N, Yoshimura S, Murotani K, Yamada T. Improved MPS-FE fluid–structure interaction coupled method with MPS polygon wall boundary model. *Comput Model Eng Sci*. 2014;4:229–47.
53. Mitsume N, Yoshimura S, Murotani K, Yamada T. MPS-FEM partitioned coupling approach for fluid–structure interaction with free surface flow. *Int J Couput Methods*. 2014;11(4):1350101.
54. Mitsume N, Yoshimura S, Murotani K, Yamada T. Inundation simulation coupling free surface flow and structures. In: *High-performance computing for structural mechanics and earthquake/tsunami engineering*. Springer; 2016; p. 179–199.
55. Farhat C, Lesoinne M. Two efficient staggered algorithms for the serial and parallel solution of three-dimensional nonlinear transient aeroelastic problems. *Comput Methods Appl Mech Eng*. 2000;182(3):499–515.
56. Mitsume N, Yoshimura S, Murotani K, Yamada T. Explicitly represented polygon wall boundary model for explicit MPS method. *Comput Particle Mech*. 2015;2(1):73–89.
57. Shakibaenia A, Jin YC. A weakly compressible MPS method for modeling of open-boundary free-surface flow. *Int J Numer Meth Fluids*. 2010;63(10):1208–32.
58. Oochi M, Koshizuka S, Sakai M. Explicit MPS algorithm for free surface flow analysis. *transactions of the Japan Society for Computational Engineering and Science*. 2010;(20120013) **(in Japanese)**.
59. Mitsume N, Yoshimura S, Yamada T. Parallel analysis system for free-surface flow using MPS with explicitly represented polygon wall boundary model. *Comput Particle Mech*. 2020;7(2):279–90.
60. Colagrossi A, Landrini M. Numerical simulation of interfacial flows by smoothed particle hydrodynamics. *J Comput Phys*. 2003;191(2):448–75.
61. Delorme L, Colagrossi A, Souto-Iglesias A, Zamora-Rodriguez R, Botia-Vera E. A set of canonical problems in sloshing, Part I: pressure field in forced roll-comparison between experimental results and SPH. *Ocean Eng*. 2009;36(2):168–78.
62. Libersky LD, Petschek AG, Carney TC, Hipp JR, Allahdadi FA. High strain Lagrangian hydrodynamics: a three-dimensional SPH code for dynamic material response. *J Comput Phys*. 1993;109(1):67–75.
63. Morris JP, Fox PJ, Zhu Y. Modeling low Reynolds number incompressible flows using SPH. *J Comput Phys*. 1997;136(1):214–26.
64. Oger G, Doring M, Alessandrini B, Ferrant P. Two-dimensional SPH simulations of wedge water entries. *J Comput Phys*. 2006;213(2):803–22.
65. Newmark NM. A method of computation for structural dynamics. *J Eng Mech Div*. 1959;85(EM3):67–94.
66. Ishihara D, Kanei S, Yoshimura S, Horie T. Efficient parallel analysis of shell-fluid interaction problem by using monolithic method based on consistent pressure Poisson equation. *J Comput Sci Technol*. 2008;2(1):185–96.
67. Minami S, Kawai H, Yoshimura S. Parallel BDD-based monolithic approach for acoustic fluid–structure interaction. *Comput Mech*. 2012;50(6):707–18.
68. Yamada T, Yoshimura S. Line search partitioned approach for fluid–structure interaction analysis of flapping wing. *Comput Model Eng Sci*. 2008;24(1):51.
69. Vacondio R, Rogers B, Stansby P. Accurate particle splitting for smoothed particle hydrodynamics in shallow water with shock capturing. *Int J Numer Meth Fluids*. 2012;69(8):1377–410.
70. Vacondio R, Rogers B, Stansby P, Mignosa P, Feldman J. Variable resolution for SPH: a dynamic particle coalescing and splitting scheme. *Comput Methods Appl Mech Eng*. 2013;256:132–48.
71. Felippa CA, Park K, Farhat C. Partitioned analysis of coupled mechanical systems. *Comput Methods Appl Mech Eng*. 2001;190(24):3247–70.
72. Matthies HG, Niekamp R, Steindorf J. Algorithms for strong coupling procedures. *Comput Methods Appl Mech Eng*. 2006;195(17):2028–49.
73. Matthies HG, Steindorf J. Partitioned strong coupling algorithms for fluid–structure interaction. *Comput Struct*. 2003;81(8):805–12.
74. Le Tallec P, Mouro J. Fluid structure interaction with large structural displacements. *Comput Methods Appl Mech Eng*. 2001;190(24):3039–67.
75. Minami S, Yoshimura S. Performance evaluation of nonlinear algorithms with line-search for partitioned coupling techniques for fluid–structure interactions. *Int J Numer Meth Fluids*. 2010;64(10–12):1129–47.
76. Walhorn E, Kölke A, Hübner B, Dinkler D. Fluid–structure coupling within a monolithic model involving free surface flows. *Comput Struct*. 2005;83(25):2100–11.
77. Idelsohn SR, Marti J, Limache A, Oñate E. Unified Lagrangian formulation for elastic solids and incompressible fluids: application to fluid–structure interaction problems via the PFEM. *Comput Methods Appl Mech Eng*. 2008;197(19):1762–76.
78. Botia Vera E, Souto Iglesias A, Bulian G, Lobovský L. Three SPH Novel Benchmark Test Cases for free surface flows. In: *Proceedings of the 5th ERCOFTAC SPHERIC workshop on SPH applications*; 2010.
79. Iglesias AS, Idelsohn S, Marti J, Rodriguez RZ, Ibáñez EO. Modeling of free surface flows with elastic bodies interactions. In: *Proceedings of the 27th Symposium on Naval Hydrodynamics*; 2008; p. 1–17.
80. Spheric benchmarks; http://canal.etsin.upm.es/ftp/SPHERIC_BENCHMARKS/, Accessed 23 Nov 2022.

Publisher's Note

Springer Nature remains neutral with regard to jurisdictional claims in published maps and institutional affiliations.